

# Tracking the Discriminative Axis: Dual Prototypes for Test-Time OOD Detection Under Covariate Shift

Wooseok Lee<sup>1</sup>, Jin Mo Yang<sup>1</sup>, Saewoong Bahk<sup>1</sup>, and Hyung-Sin Kim<sup>1</sup>

Seoul National University, Seoul, Korea

andy1ws@snu.ac.kr, jmyang@netlab.snu.ac.kr, sbahk@snu.ac.kr,  
hyungkim@snu.ac.kr

**Abstract.** For reliable deployment of deep-learning systems, out-of-distribution (OOD) detection is indispensable. In the real world, where test-time inputs often arrive as streaming mixtures of in-distribution (ID) and OOD samples under evolving covariate shifts, OOD samples are domain-constrained and bounded by the environment, and both ID and OOD are jointly affected by the same covariate factors. Existing methods typically assume a stationary ID distribution, but this assumption breaks down in such settings, leading to severe performance degradation. We empirically discover that, even under covariate shift, covariate-shifted ID (csID) and OOD (csOOD) samples remain separable along a discriminative axis in feature space. Building on this observation, we propose *DART*, a test-time, online OOD detection method that dynamically tracks dual prototypes—one for ID and the other for OOD—to recover the drifting discriminative axis, augmented with multi-layer fusion and flip correction for robustness. Extensive experiments on a wide range of challenging benchmarks, where all datasets are subjected to 15 common corruption types at severity level 5, demonstrate that our method significantly improves performance, yielding 15.32 percentage points (pp) AUROC gain and 49.15 pp FPR@95TPR reduction on ImageNet-C vs. Textures-C compared to established baselines. These results highlight the potential of the test-time discriminative axis tracking for dependable OOD detection in dynamically changing environments.

**Keywords:** OOD Detection · Covariate Shift · Online Test-time Method

## 1 Introduction

Deep neural networks (DNNs) achieve remarkable performance across applications such as image classification, object detection, medical imaging, autonomous driving, and speech recognition [1]. These successes stem from large-scale datasets, high-performance hardware, and innovative model architectures [10, 17, 28, 48], motivating deployment in real-world systems.

In practice, however, deployed models inevitably encounter test inputs that deviate from their training distributions. One form is **semantic shift**, where models

face unknown semantics—commonly termed out-of-distribution (OOD) samples. Substantial progress has been made on OOD detection: existing methods typically assume either abstract characteristics [20, 32, 53] or data-specific characteristics [29, 45] of in-distribution (ID) data to distinguish ID from OOD. A second form is **covariate shift**, where data appears under new conditions such as changes in weather, illumination, or sensor noise [12, 34]. Most OOD methods implicitly assume stationary ID distributions as reference to separate ID and OOD, however, as shown in Fig. 1, in practice they struggle under covariate shifts [55, 57, 58] because shifting covariates alter the space geometry that their decision rules rely on.

We study **test-time OOD detection under covariate shift** in a realistic *streaming mixture* setting: test-time inputs arrive in mini-batches as mixtures of ID and OOD samples, and both are simultaneously exposed to the *same evolving covariate shifts* (e.g., a change in weather). We denote these as **covariate-shifted ID (csID)** and **covariate-shifted OOD (csOOD)**. Within each mini-batch—as illustrated in Fig. 2—spatial and temporal coherence arises from the task environment, so OOD samples are *domain-constrained* rather than arbitrary. For instance, in autonomous driving, encountering an unseen vehicle type is plausible OOD, whereas suddenly observing medical or satellite images is essentially impossible. Moreover, spatio-temporally correlated csID and csOOD undergo the *same* covariate shift, so their distributions co-evolve during deployment. In our setting, the test stream is unlabeled, the backbone is frozen, no training data are accessed at test time, and the algorithm maintains a small, bounded state.

In this practical scenario, we empirically observe a key insight that enables our approach. Across diverse datasets and shifts, we consistently observe: (i) *local coherence*—within short windows, csOOD samples organize into coherent groupings in feature space; and (ii) a *recoverable linear axis*—csID and csOOD remain approximately linearly separable along a dominant discriminative direction that *drifts* as covariates evolve. As shown in Fig. 1 with annotation “Oracle”, computing our method’s OOD score with the optimal discriminative axis yields very high AUROC, demonstrating that separability in this direction can lead to strong detection performance. These observations suggest focusing on *tracking* the separation direction online rather than relying on a fixed, training-time score.

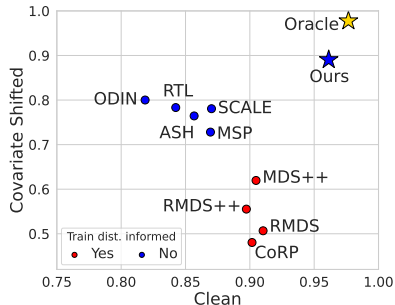


**Fig. 1:** AUROC comparison on both covariate shifted and clean ImageNet-based benchmark. Existing methods suffer under covariate shift, with train distribution-informed approaches dropping to around 0.5. In contrast, the oracle axis achieves consistently high performance regardless of shift, and our method effectively discovers this axis, attaining near-oracle results.

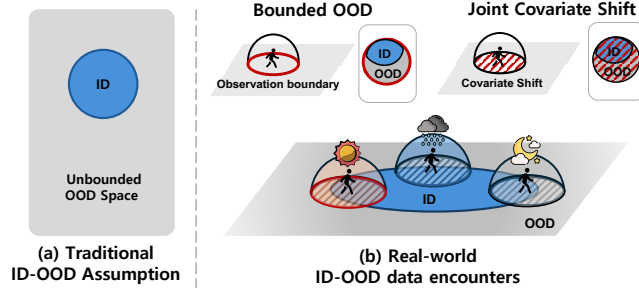


**Fig. 2:** Comparison of traditional and real-world ID-OOD assumptions. (a) Traditional OOD detection assumes ID data (blue circle) exists within an unbounded OOD space (gray background). (b) In real-world scenarios, OOD data is bounded by physical and environmental constraints (observation boundary, top-left inset), limiting the space where OOD samples can occur. Furthermore, covariate shifts such as weather conditions can simultaneously affect both ID and OOD distributions (dashed regions), causing them to shift jointly in feature space.

We propose **Discriminative Axis Real-time Tracker (*DART*)**, a **test-time, online OOD detection** method that continuously tracks a *discriminative axis* using a class-agnostic ID prototype and an OOD prototype *per feature layer*. At each step, incoming test samples update the prototypes via lightweight, stable rules, yielding the vector connecting them as the discriminative axis. Each sample is then scored by its relative position to this axis, yielding a detector aligned with the evolving feature space. To address the fact that covariate shifts affect DNN layers differently [19, 61], *DART* employs **multi-layer score fusion** to stabilize detection across heterogeneous, unpredictable shifts. The method requires only forward passes, no model weight update, no label, and no access to training data at test time, which suits privacy-sensitive or on-device deployments where retraining is infeasible. For robustness, prototypes are initialized conservatively and updated with safeguards to prevent collapse.

Across challenging benchmarks, *DART* consistently delivers substantial gains over prior approaches. For example, on the ImageNet benchmark, *DART* achieves at least **9.04 percentage points (pp)** higher AUROC under covariate shift and **5.10 pp** AUROC improvement on the clean setting, as shown in Fig. 1, while attaining **40.15 pp** and **19.06 pp** FPR@95TPR reduction on the covariate shifted and clean datasets, respectively. Notably, the performance of *DART* comes close to that of the Oracle, highlighting the effectiveness of our approach.

Our contributions can be summarized as below:

- We formalize *test-time OOD detection under covariate shift* in a streaming mixture setting, distinguishing csID from csOOD and articulating realistic constraints (data stream, frozen backbone, small memory).
- We introduce *DART*, which *tracks dual prototypes online* to recover the drifting discriminative axis and fuses *multi-layer* scores for robustness to layer-specific covariate effects.

- We provide measurements and visualizations showing coherent csOOD groupings and approximately linear csID–csOOD separation within short windows.
- We demonstrate consistent gains over strong post-hoc baselines on joint-shift suites, with large improvements in AUROC and FPR@95.

## 2 Related Work

### 2.1 Out-of-Distribution (OOD) Detection: Training-Driven vs. Post-hoc

Research on OOD detection can be broadly categorized into training-driven and post-hoc approaches.

**Training-driven approaches** modify training to enhance OOD separability, *e.g.*, Outlier Exposure (OE) with auxiliary outliers [21, 64, 68] and  $N+1$  classifiers that add an “unknown” class [5, 7, 43]. While effective, they require additional data or altered objectives and may misalign with deployment OODs, with potential side effects on ID accuracy. Some methods [25, 59] update model parameters at test time via backpropagation, which introduces latency and can compromise ID accuracy under non-stationary streams.

**Post-hoc approaches** operate on a frozen classifier without retraining and have gained widespread adoption due to their ease of use and compatibility with pretrained models. Categories include: output-based scoring [18, 20, 32], distance-based methods [29, 35, 39, 42, 45], feature-based approaches [11, 31, 44, 50, 53, 66], and gradient-based methods [4, 24]. Furthermore, *training distribution-informed* methods (*e.g.*, Mahalanobis, ViM and KNN) *assume access to training statistics* (feature means, covariances, principal subspaces)—assumptions that can become invalid under test-time covariate drift and are often infeasible when training data are unavailable. In contrast, our method is post-hoc and relies solely on the unlabeled test stream, without training statistics.

**Post-hoc, test-time adaptive approaches** are an emerging line of work which adjust OOD detection rules using test-time batches/streams *without* weight updates. RTL [14] uncovers a linear trend between OOD scores and features and fits a batch-level discriminator; OODD [60] maintains an online dynamic OOD dictionary to accumulate representative OOD features. These approaches are closer in spirit to our online setting but typically operate without explicitly addressing the time-varying covariate shift. *DART* differs by *tracking* the discriminative axis with *dual prototypes* (ID/OOD) *per layer* online across a stream; we maintain persistent, memory-light state that adapts smoothly to drift. Our goal is OOD detection under covariate drift in streaming mixtures; conventional test-time adaptation (TTA) methods that target closed-set robustness and/or adapt model weights [37, 49] are orthogonal to this objective and not our focus.

### 2.2 Covariate Shift and Joint-Shift Evaluation

**Covariate corruptions.** Covariate shift—changes in input distributions with fixed labels—is commonly studied with corruption suites such as ImageNet-C [19],

which introduce noise, blur, weather, and other factors. Recent datasets emphasize natural sources of shift from environment and sensor variation [2, 3, 26].

**Joint semantic and covariate shift.** Full-spectrum OOD [58] evaluates semantic OOD while allowing covariate variation; OpenOOD unifies large-scale OOD evaluation and includes *joint-shift* settings [56, 65]. Dataset design such as NINCO [6] reduces ID contamination for clearer semantic separation. Our setting follows this trajectory but explicitly considers *streaming mixtures* where spatio-temporally correlated csID and csOOD experience the *same evolving covariates*. *DART* is designed to adapt online in such scenarios via dual prototypes and multi-layer score fusion, without requiring training data prior or weight updates.

### 3 Method

In this section, we introduce our method *DART* for online test-time OOD detection under covariate shift. We begin by revisiting a key motivation behind our approach: the empirical emergence of discriminative axis in pre-trained feature spaces. We then describe how the prototypes that define this axis are iteratively refined with incoming test batches. Finally, we explain why multi-layer fusion is essential to maintain robustness across unpredictable types of covariate shift.

#### 3.1 Formulation Setup

We define  $\mathcal{D}_I$  and  $\mathcal{D}_O$  as the dataset for ID and OOD, observed by the OOD detection system. Then, let  $\mathcal{B}_t = \{\mathbf{x}_{t,1}, \mathbf{x}_{t,2}, \dots, \mathbf{x}_{t,N}\}$  denote an input batch received at test time, where each sample  $\mathbf{x}_{t,i}$  may belong to one of two categories under covariate shift: covariate-shifted in-distribution (csID) or covariate-shifted out-of-distribution (csOOD). We denote the subset of csID samples as  $\mathcal{B}_t^I$  and the csOOD samples as  $\mathcal{B}_t^O$ , such that  $\mathcal{B}_t = \mathcal{B}_t^I \cup \mathcal{B}_t^O$ .

Model is composed of multiple layers, and we extract intermediate feature from several of them. Let  $f_l(\cdot)$  denote the feature mapping at layer  $l$ , where  $l \in \mathcal{L} = \{1, 2, \dots, L\}$ . For a given input  $\mathbf{x}$ , we obtain a set of multi-layer features  $\{\mathbf{z}^{(1)}, \mathbf{z}^{(2)}, \dots, \mathbf{z}^{(L)}\}$ , where  $\mathbf{z}^{(l)} = f_l(\mathbf{x})$  represents the feature at layer  $l$ . Thus, for a csID sample  $\mathbf{x}_t^I \in \mathcal{B}_t^I$  and a csOOD sample  $\mathbf{x}_t^O \in \mathcal{B}_t^O$ , their multi-layer feature sets are  $\mathbf{Z}_t^I = \{\mathbf{z}_t^{(1),I}, \dots, \mathbf{z}_t^{(L),I}\}$  and  $\mathbf{Z}_t^O = \{\mathbf{z}_t^{(1),O}, \dots, \mathbf{z}_t^{(L),O}\}$ , respectively.

#### 3.2 Existence of the Discriminative Axis in Feature Space

Prior works [44, 53] have reported that ID and OOD samples exhibit distinct activation patterns in the feature space. In a similar spirit, we systematically examine unit-level activations from a distributional perspective. Specifically, we collect unit-wise activation distributions across ID and OOD samples and compare them. Our analysis reveals that there exists certain units where distributions of ID and OOD samples diverge substantially, as evidenced by a large Jensen–Shannon divergence (JSD) in Fig. 3. Visualization via violin plots further demonstrates that ID and OOD activations can be sharply distinguished within those units.

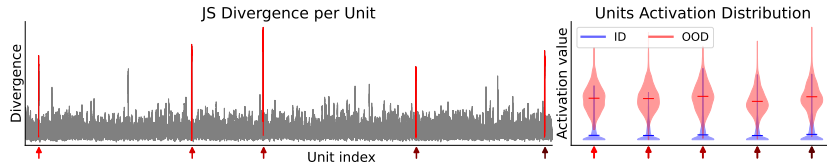


**Fig. 3:** Unit-wise activation analysis. The left panel shows the JSD between ID and OOD activations, with arrows marking units of large divergence. The right panel visualizes the activation distributions of these units, where ID (blue) and OOD (red) are clearly separable.

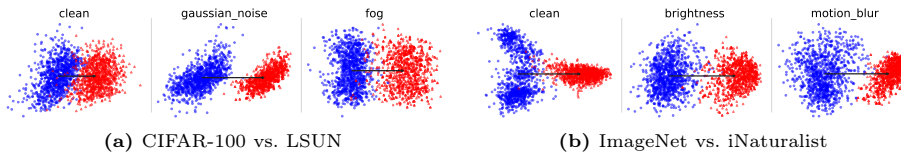


**Fig. 4:** Distribution of ID (blue dots) and OOD (red dots) samples at features space projected with the oracle discriminative axis as the horizontal axis

Building upon this insight, we leverage these distributional differences to construct a unified discriminative direction. We compute prototype representations by averaging features across all ID samples and all OOD samples respectively, yielding two representative points in the feature space<sup>1</sup>:  $\mathbf{p}_I$  and  $\mathbf{p}_O$ :

$$\mathbf{p}_I = \frac{1}{|\mathcal{D}_I|} \sum_{\mathbf{x} \in \mathcal{D}_I} f(\mathbf{x}), \quad \mathbf{p}_O = \frac{1}{|\mathcal{D}_O|} \sum_{\mathbf{x} \in \mathcal{D}_O} f(\mathbf{x}). \quad (1)$$

Then, we define the vector connecting prototypes as the **discriminative axis**:  $\mathbf{axis}_{disc}^{oracle} = \mathbf{p}_I - \mathbf{p}_O$ . This averaging implicitly weights units by their ID–OOD mean gap, emphasizing discriminative units with large mean difference and divergence while suppressing non-discriminative units. Figure 4 shows distinct ID/OOD clusters under projection onto this axis, regardless of the presence or type of covariate shift, supporting the existence of a discriminative axis.

Despite its existence, finding the discriminative axis at test time in practice is another challenge. Since the nature of OOD is inherently unknown before test-time, it is not feasible to predefine such a discriminative axis in advance. This motivates the need to adaptively identify the optimal axis during test-time. To this end, we propose a method that *progressively identifies two prototypes*—one for ID samples and the other for OOD samples—whose connecting direction defines a discriminative axis that adapts to the evolving data stream.

<sup>1</sup> While separability analysis may be conducted for each of the selected feature layers, but for clarity, we omit the layer index from the notation in this section.

### 3.3 Batch-wise Prototype Refinement: Tracking the Discriminative Axis

To craft and update the discriminative axis in an online manner, we refine prototypes through iterative pseudo-labeling and prototype updating. Refer to Appendix for the detailed algorithm.

Our method initializes and dynamically updates layer-specific prototypes for csID and csOOD based on current test batch features. Since true ID/OOD labels are unavailable during test-time, we rely on pseudo-labeling to distinguish between csID and csOOD samples. We employ Otsu algorithm [38] to automatically determine optimal thresholds by *maximizing the between-class variance*, providing a principled way to separate samples based on their score distributions.

**Dual-Prototype Initialization.** For the initial batch, we use naive baseline score, Maximum Softmax Probability (MSP) as our reference score. We assign pseudo-labels using MSP with the Otsu-determined threshold, then compute initial prototypes as the mean feature vectors of their respective pseudo-labeled groups, *i.e.*  $\bar{\mathbf{p}}_1^I = \frac{1}{|\mathcal{S}_1^I|} \sum_{i \in \mathcal{S}_1^I} f(\mathbf{x}_{1,i})$ ,  $\bar{\mathbf{p}}_1^O = \frac{1}{|\mathcal{S}_1^O|} \sum_{i \in \mathcal{S}_1^O} f(\mathbf{x}_{1,i})$ .

**Dual-Prototype Tracking.** For subsequent batches, we repeat the following steps to obtain a more refined OOD score that leverages the built prototypes. We *(i)* compute Euclidean distances between each sample from current batch and the dual prototypes from the previous timestep, then *(ii)* calculate a Relative Distance Score (RDS) that reflects each sample’s position relative to both prototypes:

$$\text{RDS}(\mathbf{x}_{t,i}) = 1 - \frac{\|\mathbf{z}_{t,i} - \bar{\mathbf{p}}_{t-1}^I\|_2}{\|\mathbf{z}_{t,i} - \bar{\mathbf{p}}_{t-1}^I\|_2 + \|\mathbf{z}_{t,i} - \bar{\mathbf{p}}_{t-1}^O\|_2}, \quad (2)$$

where  $\mathbf{z}_{t,i}$  denotes the feature of  $i$ -th sample in the batch  $t$ . The RDS formulation is inherently scale-invariant, making it robust to variations in feature magnitudes across different layers and models. Next, using Otsu algorithm, we *(iii)* determine a threshold to assign pseudo-labels based on this RDS score. We *(iv)* apply Tukey’s *outlier filtering* [46] to exclude samples that lie too far from their assigned prototypes, and then *(v)* compute new  $\hat{\mathbf{p}}_t^{\text{ID}}$  and  $\hat{\mathbf{p}}_t^{\text{OOD}}$  as the mean feature of the remaining pseudo-labeled groups. Tukey-based filtering improves prototype reliability by excluding unreliable samples from the mean computation. Finally, we *(vi)* refine prototypes using *exponential moving average* to maintain stability:

$$\bar{\mathbf{p}}_t^I = \alpha \bar{\mathbf{p}}_{t-1}^I + (1 - \alpha) \hat{\mathbf{p}}_t^I, \quad \bar{\mathbf{p}}_t^O = \alpha \bar{\mathbf{p}}_{t-1}^O + (1 - \alpha) \hat{\mathbf{p}}_t^O. \quad (3)$$

This iterative process enables prototypes to progressively converge toward the true underlying distributions and identify a near-optimal discriminative axis.

**Flip Correction.** Due to *DART*’s pseudo-labeling approach, incorrectly initialized prototypes can lead to catastrophic misplacement, with prototypes potentially drifting toward opposite sides of their desirable locations. To address this, every  $k$ -th batches, we perform a “flip” detection mechanism that identifies prototype misalignments and automatically swaps them when necessary. We detect flips by comparing current prototypes with an auxiliary MSP-based

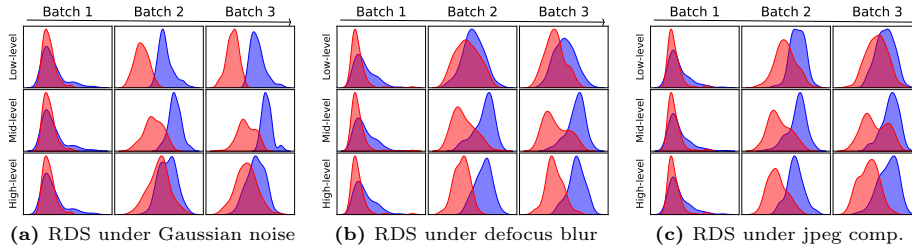


**Fig. 5:** Layer-wise RDS distributions across three covariate shift types. Each plot shows the RDS distribution of **csID** (blue curve, CIFAR-100) and **csOOD** (red curve, LSUN) samples at different network depths (low, mid, high-level) through three sequential batches. The visualizations reveal how different corruption types affect feature separability at specific network layers; under Gaussian noise, separability degrades in high-level layers, whereas under defocus blur, it degrades in low-level layers.

prototype, *i.e.*  $\hat{\mathbf{p}}_{t,M}^I$  and  $\hat{\mathbf{p}}_{t,M}^O$ . A flip occurs when the csID prototype is significantly farther from the MSP-based reference than the csOOD prototype, while simultaneously showing lower cosine similarity. Formally, we swap prototypes if

$$\|\bar{\mathbf{p}}_t^I - \hat{\mathbf{p}}_{t,M}^I\|_2 > 2\|\bar{\mathbf{p}}_t^O - \hat{\mathbf{p}}_{t,M}^O\|_2 \quad \text{and} \quad \cos(\bar{\mathbf{p}}_t^I, \hat{\mathbf{p}}_{t,M}^I) < \cos(\bar{\mathbf{p}}_t^O, \hat{\mathbf{p}}_{t,M}^O). \quad (4)$$

We use a weighted comparison (factor of 2) to impose a strict condition preventing unintended flip detections, and a value we found works well across all datasets.

### 3.4 Multi-Layer Score Fusion

To enhance discriminative axis identification, we extend our approach to multi-layer features. Low-level features capture local patterns like textures and edges, while high-level features encode semantic concepts [16]. However, covariate shifts can selectively disrupt different levels of visual information [19, 61]—blur corruptions primarily affect low-level features, while elastic transformations impair higher-level representations. As a result, different layers exhibit varying degrees of ID/OOD discriminability depending on the shift type, as illustrated in Fig. 5. Since the nature of covariate shift is typically *unknown beforehand*, leveraging information from all feature levels through multi-layer fusion is essential for robust OOD detection.

As the prototypes are updated for each batch, we compute the  $RDS_l$  for each selected layer  $l$ . To obtain the final OOD score for each sample  $\mathbf{x}_{t,i}$  in the batch, we fuse the RDS values from the selected layers  $\mathcal{L}$  by taking their *average*, formally given by  $RDS_{\text{final}}(\mathbf{x}_{t,i}) = \frac{1}{|\mathcal{L}|} \sum_{l \in \mathcal{L}} RDS_l(\mathbf{x}_{t,i})$ . Using the fused OOD score  $RDS_{\text{final}}(\mathbf{x}_{t,i})$ , we make the final OOD prediction.

**Table 1:** OOD detection performance with CIFAR-100-C and ImageNet-C csID. Results are the average of all 15 corruptions. (Best: **bolded**, Second-best: underlined)

ImageNet-C													
Method	Training set prior	ImageNet-O-C		Places-C		SUN-C		iNaturalist-C		Textures-C		Average	
		FPR95 ↓ AUROC ↑											
MSP	NO	85.01	62.18	74.41	73.10	73.64	73.65	53.91	82.27	70.88	72.85	71.57	72.81
Energy	NO	82.68	63.65	70.13	77.66	69.70	78.79	59.45	82.48	62.58	78.16	68.91	76.13
Max logit	NO	83.69	63.51	71.00	76.64	70.11	77.59	53.19	83.76	65.85	76.85	68.77	75.67
GradNorm	NO	85.09	58.28	68.15	78.13	64.77	81.23	49.29	85.45	<u>51.70</u>	<u>84.11</u>	63.80	77.44
ViM	YES	91.28	54.02	98.75	25.72	99.14	23.46	99.41	18.87	97.90	29.31	97.30	30.28
KNN	YES	92.60	53.73	98.17	30.68	98.23	29.94	98.69	24.10	90.21	50.39	95.58	37.77
MDS <sub>single</sub>	YES	92.67	50.34	99.11	21.17	99.40	18.89	99.68	14.49	98.29	26.37	97.83	26.25
MDS <sub>ensemble</sub>	YES	85.89	58.76	98.08	27.51	98.23	26.49	98.31	21.40	81.15	47.73	92.33	36.38
ODIN	NO	86.67	59.91	<u>57.03</u>	<u>83.67</u>	<u>54.88</u>	<u>84.53</u>	44.03	<u>88.03</u>	53.95	83.93	<u>59.31</u>	<u>80.01</u>
ReAct	YES	90.46	54.69	89.30	66.71	88.96	68.19	92.42	64.03	86.26	66.59	89.48	64.04
SCALE	NO	<u>82.06</u>	65.18	67.20	79.03	65.58	80.33	48.40	85.75	60.80	80.03	64.81	78.06
ASH	NO	82.45	63.90	69.82	77.91	69.26	79.08	58.88	82.76	62.00	78.55	68.48	76.44
RTL	NO	83.70	<u>65.26</u>	65.44	79.96	64.27	80.32	<u>41.39</u>	87.69	64.08	78.36	63.78	78.32
NNGuide	YES	88.94	56.31	81.97	69.88	81.05	73.03	74.75	76.53	58.93	79.60	77.13	71.07
CoRP	YES	93.02	52.30	95.18	46.32	95.22	46.33	95.99	43.54	93.05	51.72	94.49	48.04
MDS++	YES	82.39	64.35	90.03	52.53	90.68	52.72	64.23	71.61	66.93	68.57	78.85	61.96
RMDS	YES	92.91	58.76	96.74	48.73	97.50	47.40	95.35	53.60	96.64	44.86	95.83	50.69
RMDS++	YES	94.61	57.05	96.02	52.76	96.38	51.52	93.87	64.11	95.33	52.20	95.24	55.53
<i>DART</i>	NO	<b>68.87</b>	<b>66.63</b>	<b>8.70</b>	<b>92.96</b>	<b>8.08</b>	<b>93.03</b>	<b>7.60</b>	<b>93.18</b>	<b>2.55</b>	<b>99.43</b>	<b>19.16</b>	<b>89.05</b>
CIFAR-100-C													
Method	Training set prior	SVHN-C		Places365-C		LSUN-C		iSUN-C		Textures-C		Average	
		FPR95 ↓ AUROC ↑											
MSP	NO	91.48	58.40	87.30	64.23	86.85	64.49	88.40	62.74	91.91	58.24	89.19	61.62
Energy	NO	93.13	60.53	84.74	66.56	84.04	68.57	87.14	64.79	90.20	61.10	87.85	64.31
Max logit	NO	92.73	60.58	85.04	66.43	84.43	68.24	87.15	64.74	90.74	60.78	88.02	64.15
GradNorm	NO	96.07	47.75	92.56	52.99	94.89	45.14	94.79	45.32	84.59	62.52	92.58	50.74
ViM	YES	77.24	72.64	90.23	59.74	86.41	64.41	87.65	62.40	93.15	55.11	86.94	62.86
KNN	YES	88.45	66.38	85.63	63.99	83.87	70.22	87.06	65.25	90.83	60.93	87.17	65.35
MDS <sub>single</sub>	YES	89.04	61.64	91.30	57.42	84.94	65.60	86.68	62.82	95.16	48.58	89.42	59.21
MDS <sub>ensemble</sub>	YES	<u>63.57</u>	79.33	92.49	48.49	<u>73.78</u>	60.77	<u>73.95</u>	58.87	75.16	57.51	<u>75.79</u>	60.99
ODIN	NO	79.07	70.05	88.23	63.54	89.96	59.13	90.48	59.18	77.69	70.79	85.09	64.54
ReAct	YES	95.08	55.32	88.78	62.51	86.39	67.46	88.07	64.76	91.90	60.40	90.04	62.09
SCALE	NO	88.88	66.46	85.55	<u>66.91</u>	86.30	65.89	88.06	64.21	81.14	70.69	85.99	66.83
ASH	NO	92.05	62.73	85.42	66.48	85.24	67.78	87.99	64.30	87.66	64.61	87.67	65.18
RTL	NO	89.27	58.60	<u>84.59</u>	64.62	83.65	66.99	86.90	63.60	89.30	57.65	86.74	62.29
NNGuide	YES	91.11	62.78	88.78	63.45	91.30	58.64	91.96	57.62	77.91	68.69	88.21	62.24
CoRP	YES	64.51	<b>80.52</b>	89.98	60.28	92.56	59.80	91.30	59.91	<u>55.25</u>	<b>81.49</b>	78.72	<u>68.40</u>
MDS++	YES	95.15	62.58	87.40	64.87	87.25	66.75	89.85	62.90	95.16	59.59	90.96	63.34
RMDS	YES	88.78	64.07	86.67	64.65	79.57	<u>71.82</u>	82.68	<u>67.91</u>	94.23	55.06	86.39	64.70
RMDS++	YES	91.52	65.51	85.70	65.59	82.73	70.26	86.08	66.38	93.78	58.41	87.96	65.23
<i>DART</i>	NO	<b>48.60</b>	<u>79.82</u>	<b>68.66</b>	<b>68.00</b>	<u>44.14</u>	<b>80.29</b>	<b>50.76</b>	<b>79.75</b>	<b>51.48</b>	<u>80.60</u>	<b>52.73</b>	<b>77.69</b>

## 4 Experiments

### 4.1 Experimental Setup

**Evaluation Details.** Although *DART* is designed to adaptively handle challenging covariate shifts, we evaluate on both clean and covariate-shifted datasets as the shift may be weak or absent in real-world scenarios. We use CIFAR-100 [27] and ImageNet [10] as ID datasets. For CIFAR-100, we use SVHN [36], Places365 [67], LSUN [62], iSUN [54], and Textures [8] as OOD sets. For ImageNet, we use ImageNet-O [23], Places [67], SUN [52], iNaturalist [47], and Textures. To simulate covariate shift, we apply 15 common corruption types [19] at severity level 5 to both ID and OOD datasets, resulting in pairs such as CIFAR-100-C vs. SVHN-C. In our main evaluations, each test-time batch contains an equal number of ID/OOD samples, and we report results under varying ID/OOD ratios in Appendix. For CIFAR-100-based benchmarks, we use WideResNet-40-2 [63] pre-trained with AugMix [22] on CIFAR-100, which is available from RobustBench [9].

For ImageNet-based benchmarks, we use the pre-trained RegNetY-16GF [41] available from PyTorch. In addition, we also evaluate with Transformer-based models on CIFAR-100, all of which are fine-tuned with CIFAR-100. Results with pre-trained ResNet-50 [17] on ImageNet are also provided in Appendix.

**Baseline Methods.** MSP [20], Max Logit [18], Energy [32], ODIN [31], Grad-Norm [24], SCALE [53], ASH [11], and RTL [14], like *DART*, do not require any precomputed statistics or storage from the training data, whereas KNN [45], ViM [50], ReAct [44], NNGuide [39], CoRP [15], MDS [29] and its variants [35, 42] do. As MDS has been implemented in prior work using either single-layer or multi-layer, we compare against both variants.

## 4.2 Main OOD Detection Results

**Results on Covariate Shifted Dataset.** As *DART* is designed to adapt to test-time covariate shift, it demonstrates its full potential in the covariate-shifted setting. As shown in Tab. 1, on ImageNet-C benchmark, *DART* achieves the best performance on every OOD dataset and both evaluation metrics, with an average FPR@95TPR (FPR95) reduction of **40.15 pp** and average AUROC gain of **9.04 pp** compared to the second-best (*i.e.*, ODIN). On CIFAR-100-C, *DART* again achieves the best performance: an average FPR95 reduction of **23.06 pp** relative to MDS and an AUROC gain of **9.29 pp** upon CoRP. These results highlight the robustness and adaptability of *DART* in the face of test-time covariate shift. An important observation is that methods using prior information from training set tend to perform similarly to, or *even worse* than, baselines that do not use such priors. This suggests that the prior information which is typically beneficial for OOD detection on clean datasets may become misaligned with test-time distributions under covariate shift, leading to degraded performance.

**Results on Clean Dataset.** Table 2 reports the OOD detection performance on the clean CIFAR-100 and ImageNet benchmark. Although *DART* mainly targets covariate-shifted environments, it consistently outperforms all baselines on the clean benchmarks, achieving the lowest average FPR95 and the highest average AUROC. *DART* reduces FPR95 by **19.06 pp** compared to SCALE on ImageNet and **12.72 pp** relative to MDS on CIFAR-100, while improving AUROC by **5.10 pp** over RMDS and **3.42 pp** against MDS, respectively. These results suggest that ID and OOD samples are well-separated in the feature space and that the ID and OOD prototypes are finely adjusted by *DART* toward

**Table 2:** OOD detection performance without covariate shift. All results are reported as the mean over all five OOD datasets for each ID set. (Best: **bolded**, Second-best: underlined)

Method	ImageNet		CIFAR-100	
	FPR95 ↓	AUROC ↑	FPR95 ↓	AUROC ↑
MSP	44.64	86.94	80.37	75.29
Energy	38.25	85.52	79.95	76.79
Max logit	37.05	86.43	79.91	77.06
GradNorm	80.50	57.26	94.92	43.62
ViM	56.58	87.60	71.94	75.61
KNN	84.79	75.87	71.48	81.16
MDS <sub>single</sub>	79.19	80.57	80.01	69.98
MDS <sub>ensemble</sub>	55.30	86.86	<u>45.94</u>	<u>86.36</u>
ODIN	60.84	81.86	81.11	69.50
ReAct	86.40	70.67	79.45	76.09
SCALE	<u>35.01</u>	87.02	76.60	77.53
ASH	37.77	85.67	80.44	76.76
RTL	42.30	84.24	64.11	80.76
NNGuide	70.60	70.05	87.55	66.29
CoRP	49.03	90.17	65.54	81.05
MDS++	41.87	90.48	85.96	75.52
RMDS	46.28	<u>91.03</u>	67.90	82.51
RMDS++	56.01	89.73	73.91	81.57
<i>DART</i>	<b>15.95</b>	<b>96.13</b>	<b>33.12</b>	<b>89.78</b>

**Table 3:** OOD detection performance comparison with ViT-Tiny and Swin-T architectures. All results are reported as the mean over all five OOD datasets. For covariate shifted datasets, results are the average of all 15 corruptions with severity level 5. (Best: **bolded**, Second-best: underlined)

Method	Training set prior	Covariate shifted				Clean			
		ViT-Tiny		Swin-T		ViT-Tiny		Swin-T	
		FPR95 ↓	AUROC ↑	FPR95 ↓	AUROC ↑	FPR95 ↓	AUROC ↑	FPR95 ↓	AUROC ↑
MSP	NO	89.56	57.03	85.24	63.39	70.36	79.79	60.16	84.31
Energy	NO	87.01	61.20	80.30	68.35	58.77	84.83	41.06	89.80
Max Logit	NO	87.58	60.65	81.90	67.73	60.27	84.54	42.11	89.52
GradNorm	NO	89.54	58.42	78.77	71.44	78.33	75.24	71.63	74.53
ViM	YES	89.49	58.75	96.94	45.76	58.27	85.06	93.00	66.26
KNN	YES	90.15	56.81	84.25	64.91	67.35	79.58	45.93	88.51
MDS <sub>single</sub>	YES	97.22	32.40	98.76	33.09	96.38	35.57	98.67	41.11
MDS <sub>ensemble</sub>	YES	<u>61.73</u>	65.95	98.60	33.75	<u>29.18</u>	<u>88.40</u>	98.42	45.53
ODIN	NO	87.53	60.52	84.88	63.63	80.25	71.22	91.20	63.65
ReAct	YES	85.94	62.01	76.76	71.14	56.86	81.79	41.78	89.51
SCALE	NO	88.84	58.99	76.68	71.57	61.75	83.66	44.84	88.50
ASH	NO	92.00	56.00	76.95	71.39	81.17	74.00	50.03	86.97
RTL	NO	84.42	58.69	83.71	63.62	40.20	87.75	50.90	84.23
NNGuide	YES	86.49	61.17	76.53	<u>73.38</u>	60.30	83.43	38.04	<u>91.06</u>
CoRP	YES	88.31	59.85	86.17	63.65	67.28	82.43	50.37	88.53
MDS++	YES	79.15	<u>66.25</u>	<u>76.01</u>	69.80	46.70	87.12	<u>35.28</u>	<b>91.54</b>
RMDS	YES	82.63	63.56	91.33	58.14	47.98	86.93	54.00	87.65
RMDS++	YES	81.30	64.05	88.13	61.81	48.11	86.71	47.01	88.90
<i>DART</i>	NO	<b>44.28</b>	<b>68.60</b>	<b>38.90</b>	<b>81.28</b>	<b>20.58</b>	<b>94.31</b>	<b>31.86</b>	88.03

optimal axis for discrimination. Notably, baselines that leverage prior information from training set tend to outperform those not relying on such information. *DART* defies this trend, performing the best without any prior information.

**Results with Transformer Architectures.** We also evaluate with transformer-based architectures [48], specifically ViT-Tiny [13, 51] and Swin-T [33], to verify robustness across different model architectures. As shown in Tab. 3, *DART* outperforms all baselines, yielding FPR95 drop of **17.45 pp** (covariate-shifted) and **8.6 pp** (clean) against the second-best method (*i.e.*, MDS) with ViT-Tiny. Similarly, for Swin-T, *DART* reduces FPR95 by **37.11 pp** (covariate-shifted) and **3.42 pp** (clean) relative to MDS++. This proves the superiority of *DART* and the emergence of discriminative axis regardless of the model architecture.

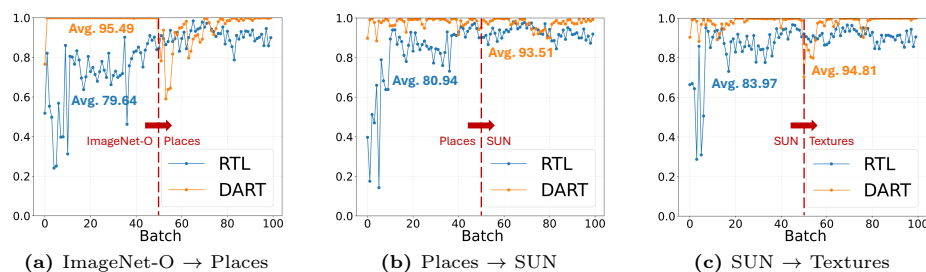
### 4.3 Cross-domain Evaluation Results

In the previous experiments, each test stream contains a single OOD dataset and a single type of covariate shift. We further evaluate *DART* in more challenging regimes with multiple OOD datasets and multiple covariate shifts. All cross-domain evaluations use ImageNet as the ID and ResNet-50 as the backbone.

**Mixed OOD.** We believe our bounded OOD setting reflects realistic deployment scenarios where OOD inputs tend to concentrate within a limited semantic space

**Table 4:** Mixed OOD evaluation

Method	ImageNet-O + Places		Places + SUN		SUN + Textures	
	FPR95 ↓	AUROC ↑	FPR95 ↓	AUROC ↑	FPR95 ↓	AUROC ↑
MSP	48.43	83.70	48.65	84.26	43.65	85.52
Energy	51.56	78.42	44.24	82.57	38.31	85.65
Max Logit	48.14	80.20	42.85	83.49	37.29	86.24
GradNorm	86.49	43.25	77.26	57.44	67.54	66.80
ODIN	62.28	79.44	66.10	76.78	60.37	80.13
SCALE	47.62	80.09	40.36	84.39	33.92	87.81
RTL	46.82	81.46	44.77	82.94	40.64	83.98
<b>DART</b>	<b>19.23</b>	<b>94.45</b>	<b>25.96</b>	<b>91.15</b>	<b>18.65</b>	<b>94.80</b>

**Fig. 6:** Continual OOD evaluation: AUROC vs. batch

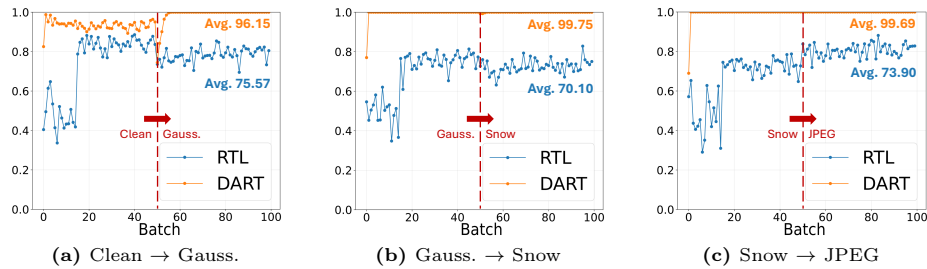
due to observation boundaries. However, to further show robustness *beyond this assumption*, we conducted additional experiments where two different OOD sources are *mixed* simultaneously. At each batch, OOD samples are drawn from two diverse sources rather than a single dataset. In Tab. 4, *DART* remains best even under mixed OOD, indicating that our OOD prototype successfully finds the discriminative axis even when OOD samples span multiple semantic categories. We observe performance degradation only in an extreme case where all five OOD sets are mixed. However, we believe such extreme mixing rarely occurs in practice, and our assumption holds within realistic deployment boundaries.

**Continual OOD.** We also consider a continual-OOO stream where the OOD source *changes* abruptly across temporal segments while the ID stream remains fixed. Since this setting is designed to evaluate online adaptation capability, we only include methods that adapt online. Results in Fig. 6 show that *DART* remains stable across segments, with only modest fluctuations at switch points, indicating that our prototype-based tracking can re-estimate the relevant axis over time.

**Mixed Covariate Shift.** We further test streams where each batch contains data from multiple covariate shifts, considering mixtures of two shifts and mixture of all 15 shifts. As shown in Tab. 5, *DART* consistently surpasses all baselines under mixed shifts, remaining best even in the extreme mixture-of-15 setting.

**Table 5:** Mixed covariate shift evaluation

Method	Clean + Gauss.		Gauss. + Snow		Snow + JPEG		All 15 corruptions	
	FPR95 ↓	AUROC ↑	FPR95 ↓	AUROC ↑	FPR95 ↓	AUROC ↑	FPR95 ↓	AUROC ↑
MSP	82.63	67.43	85.01	62.49	83.07	68.22	86.64	62.71
Energy	72.01	76.77	83.91	69.82	89.72	66.83	86.27	63.02
Max Logit	77.19	73.34	85.40	67.10	85.73	68.66	86.46	63.67
GradNorm	54.72	83.51	65.33	81.94	72.16	79.49	69.55	77.45
ODIN	66.85	77.72	45.20	83.46	12.08	97.39	25.45	92.16
SCALE	66.99	78.21	80.27	71.68	79.15	73.94	78.20	71.19
RTL	79.84	67.73	81.92	65.32	79.86	71.65	81.27	65.63
<b>DART</b>	<b>22.04</b>	<b>93.93</b>	<b>0.85</b>	<b>99.62</b>	<b>0.79</b>	<b>99.72</b>	<b>19.68</b>	<b>92.70</b>

**Fig. 7:** Continual covariate shift evaluation: AUROC vs. batch

**Continual Covariate Shift.** Finally, we evaluate continual covariate shift where the corruption type evolves over time while samples within each segment remain temporally correlated. As in the continual OOD setting, we only include online methods. In Fig. 7, *DART* maintains strong performance after corruption change.

#### 4.4 Ablation Studies

**Progression of Axis-Alignment.** Figure 8 demonstrates the online convergence capability of *DART* in discovering the oracle discriminative axis. The stars denote the global ID/OOD centroids, whose connecting line is the oracle axis, while the triangles denote batch-wise ID/OOD prototypes estimated by *DART*, whose connecting line is the online axis. The cosine similarity between two axes increases across batches, demonstrating *DART*'s ability to navigate the high-dimensional feature space and progressively align with the true discriminative direction.

**Impact of Multi-layer Fusion.** Figure 9a compares full *DART* against its single-layer variants on CIFAR-100 vs. LSUN, demonstrating the impact of multi-layer fusion. While *DART* achieves the highest average performance, the key advantage lies in *stability*. Single-layer variants occasionally outperform *DART* in specific settings (*e.g.*, Block3 on clean data, Block1 under Gaussian noise) but exhibit catastrophic failures under other corruptions due to varying covariate-shift impacts across layers. Therefore, *DART*'s multi-layer ensemble provides robustness under diverse covariate shifts.

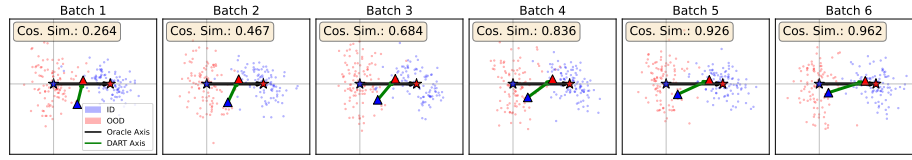


**Fig. 8:** Progression of axis alignment at CIFAR-100-C vs. LSUN-C under impulse noise

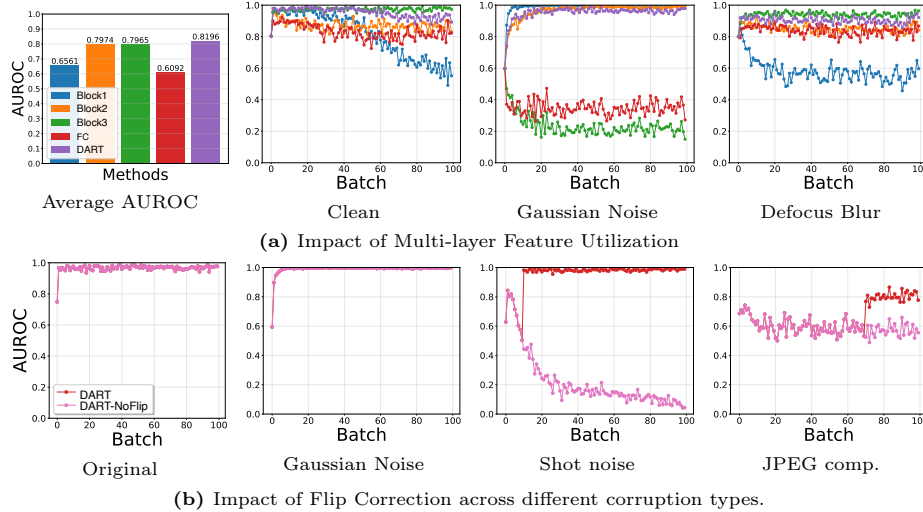


**Fig. 9:** Impact of *DART*'s individual components

**Impact of Flip Correction.** Figure 9b demonstrates the critical role of *DART*'s flip correction. We compare *DART* with *DART*-NoFlip (without flip correction) on CIFAR-100 vs. iSUN for original and corrupted datasets. While both perform identically on original data and under Gaussian noise, Shot noise reveals a drastic difference. Standard *DART* recovers via prototype flip and performs robustly, while *DART*-NoFlip suffers catastrophic degradation of detection capability due to reversed prototypes under Shot noise. The flip correction detects and rectifies these inversions by ensuring consistent prototype proximity. Similar effects with JPEG compression further validate the effectiveness.

## 5 Conclusion

In this work, we addressed the realistic challenge of OOD detection under test-time covariate shift, a scenario where existing methods often collapse. Our analysis revealed the consistent existence of a discriminative axis along which covariate-shifted ID and OOD samples remain separable. Building on this insight, we proposed *DART*, which dynamically tracks prototypes to recover the evolving discriminative axis with multi-layer fusion. Extensive experiments across diverse

datasets and architectures confirmed its superiority over strong baselines, underscoring the promise of prototype-based axis tracking as a practical solution for reliable OOD detection in real-world environments.

**Limitations and Future Works.** While *DART* demonstrates strong performance, several avenues remain for improvement. The reliance on MSP-based initialization may impact performance when initial pseudo-labeling quality is poor, suggesting a need for more robust initialization strategies. Additionally, extending *DART* beyond vision tasks to other modalities presents an opportunity to validate the universality of discriminative axis tracking across different data representations.

## References

1. Alam, M., Samad, M.D., Vidyaratne, L., Glandon, A., Iftekharuddin, K.M.: Survey on deep neural networks in speech and vision systems. *Neurocomputing* **417**, 302–321 (2020)
2. Baek, E., Han, S.h., Gong, T., Kim, H.S.: Adaptive camera sensor for vision models. In: *The Thirteenth International Conference on Learning Representations* (2025)
3. Baek, E., Park, K., Kim, J., Kim, H.S.: Unexplored faces of robustness and out-of-distribution: Covariate shifts in environment and sensor domains. In: *Proceedings of the IEEE/CVF Conference on Computer Vision and Pattern Recognition*. pp. 22294–22303 (2024)
4. Behpour, S., Doan, T.L., Li, X., He, W., Gou, L., Ren, L.: Gradorth: A simple yet efficient out-of-distribution detection with orthogonal projection of gradients. *Advances in Neural Information Processing Systems* **36**, 38206–38230 (2023)
5. Bendale, A., Boulton, T.E.: Towards open set deep networks. In: *Proceedings of the IEEE conference on computer vision and pattern recognition*. pp. 1563–1572 (2016)
6. Bitterwolf, J., Müller, M., Hein, M.: In or out? fixing imagenet out-of-distribution detection evaluation. In: *International Conference on Machine Learning*. pp. 2471–2506. PMLR (2023)
7. Chen, G., Peng, P., Wang, X., Tian, Y.: Adversarial reciprocal points learning for open set recognition. *IEEE Transactions on Pattern Analysis and Machine Intelligence* **44**(11), 8065–8081 (2021)
8. Cimpoi, M., Maji, S., Kokkinos, I., Mohamed, S., Vedaldi, A.: Describing textures in the wild. In: *Proceedings of the IEEE conference on computer vision and pattern recognition*. pp. 3606–3613 (2014)
9. Croce, F., Andriushchenko, M., Schwag, V., Debnedetti, E., Flammarion, N., Chiang, M., Mittal, P., Hein, M.: Robustbench: a standardized adversarial robustness benchmark. *arXiv preprint arXiv:2010.09670* (2020)
10. Deng, J., Dong, W., Socher, R., Li, L.J., Li, K., Fei-Fei, L.: Imagenet: A large-scale hierarchical image database. In: *2009 IEEE conference on computer vision and pattern recognition*. pp. 248–255. Ieee (2009)
11. Djuricic, A., Bozanic, N., Ashok, A., Liu, R.: Extremely simple activation shaping for out-of-distribution detection. *arXiv preprint arXiv:2209.09858* (2022)
12. Dockès, J., Varoquaux, G., Poline, J.B.: Preventing dataset shift from breaking machine-learning biomarkers. *GigaScience* **10**(9), giab055 (2021)
13. Dosovitskiy, A., Beyer, L., Kolesnikov, A., Weissenborn, D., Zhai, X., Unterthiner, T., Dehghani, M., Minderer, M., Heigold, G., Gelly, S., Uszkoreit, J., Houlsby, N.:

- An image is worth 16x16 words: Transformers for image recognition at scale. In: International Conference on Learning Representations (2021)
14. Fan, K., Liu, T., Qiu, X., Wang, Y., Huai, L., Shanguan, Z., Gou, S., Liu, F., Fu, Y., Fu, Y., et al.: Test-time linear out-of-distribution detection. In: Proceedings of the IEEE/CVF Conference on Computer Vision and Pattern Recognition. pp. 23752–23761 (2024)
  15. Fang, K., Tao, Q., Lv, K., He, M., Huang, X., Yang, J.: Kernel pca for out-of-distribution detection. *Advances in Neural Information Processing Systems* **37**, 134317–134344 (2024)
  16. Guo, Y., Liu, Y., Oerlemans, A., Lao, S., Wu, S., Lew, M.S.: Deep learning for visual understanding: A review. *Neurocomputing* **187**, 27–48 (2016)
  17. He, K., Zhang, X., Ren, S., Sun, J.: Deep residual learning for image recognition. In: Proceedings of the IEEE conference on computer vision and pattern recognition. pp. 770–778 (2016)
  18. Hendrycks, D., Basart, S., Mazeika, M., Zou, A., Kwon, J., Mostajabi, M., Steinhardt, J., Song, D.: Scaling out-of-distribution detection for real-world settings. arXiv preprint arXiv:1911.11132 (2019)
  19. Hendrycks, D., Dietterich, T.: Benchmarking neural network robustness to common corruptions and perturbations. arXiv preprint arXiv:1903.12261 (2019)
  20. Hendrycks, D., Gimpel, K.: A baseline for detecting misclassified and out-of-distribution examples in neural networks. arXiv preprint arXiv:1610.02136 (2016)
  21. Hendrycks, D., Mazeika, M., Dietterich, T.: Deep anomaly detection with outlier exposure. arXiv preprint arXiv:1812.04606 (2018)
  22. Hendrycks, D., Mu, N., Cubuk, E.D., Zoph, B., Gilmer, J., Lakshminarayanan, B.: Augmix: A simple data processing method to improve robustness and uncertainty. arXiv preprint arXiv:1912.02781 (2019)
  23. Hendrycks, D., Zhao, K., Basart, S., Steinhardt, J., Song, D.: Natural adversarial examples. In: Proceedings of the IEEE/CVF conference on computer vision and pattern recognition. pp. 15262–15271 (2021)
  24. Huang, R., Geng, A., Li, Y.: On the importance of gradients for detecting distributional shifts in the wild. *Advances in Neural Information Processing Systems* **34**, 677–689 (2021)
  25. Katz-Samuels, J., Nakhleh, J.B., Nowak, R., Li, Y.: Training ood detectors in their natural habitats. In: International Conference on Machine Learning. pp. 10848–10865. PMLR (2022)
  26. Kim, J.y., Baek, E., Kim, H.S.: Imagenet-ses: A first systematic study of sensor-environment simulation anchored by real recaptures. In: Proceedings of the IEEE/CVF Winter Conference on Applications of Computer Vision. pp. 1117–1126 (2026)
  27. Krizhevsky, A., Hinton, G., et al.: Learning multiple layers of features from tiny images (2009)
  28. Krizhevsky, A., Sutskever, I., Hinton, G.E.: Imagenet classification with deep convolutional neural networks. *Advances in neural information processing systems* **25** (2012)
  29. Lee, K., Lee, K., Lee, H., Shin, J.: A simple unified framework for detecting out-of-distribution samples and adversarial attacks. *Advances in neural information processing systems* **31** (2018)
  30. Liang, S., Li, Y., Srikant, R.: Enhancing the reliability of out-of-distribution image detection in neural networks. In: International Conference on Learning Representations (2018), <https://openreview.net/forum?id=H1VGkIxRZ>

31. Liang, S., Li, Y., Srikant, R.: Enhancing the reliability of out-of-distribution image detection in neural networks. arXiv preprint arXiv:1706.02690 (2017)
32. Liu, W., Wang, X., Owens, J., Li, Y.: Energy-based out-of-distribution detection. *Advances in neural information processing systems* **33**, 21464–21475 (2020)
33. Liu, Z., Lin, Y., Cao, Y., Hu, H., Wei, Y., Zhang, Z., Lin, S., Guo, B.: Swin transformer: Hierarchical vision transformer using shifted windows. In: *Proceedings of the IEEE/CVF international conference on computer vision*. pp. 10012–10022 (2021)
34. Moreno-Torres, J.G., Raeder, T., Alaiz-Rodríguez, R., Chawla, N.V., Herrera, F.: A unifying view on dataset shift in classification. *Pattern recognition* **45**(1), 521–530 (2012)
35. Mueller, M., Hein, M.: Mahalanobis++: Improving ood detection via feature normalization. arXiv preprint arXiv:2505.18032 (2025)
36. Netzer, Y., Wang, T., Coates, A., Bissacco, A., Wu, B., Ng, A.Y., et al.: Reading digits in natural images with unsupervised feature learning. In: *NIPS workshop on deep learning and unsupervised feature learning*. vol. 2011, p. 4. Granada (2011)
37. Niu, S., Wu, J., Zhang, Y., Wen, Z., Chen, Y., Zhao, P., Tan, M.: Towards stable test-time adaptation in dynamic wild world. arXiv preprint arXiv:2302.12400 (2023)
38. Otsu, N., et al.: A threshold selection method from gray-level histograms. *Automatica* **11**(285-296), 23–27 (1975)
39. Park, J., Jung, Y.G., Teoh, A.B.J.: Nearest neighbor guidance for out-of-distribution detection. In: *Proceedings of the IEEE/CVF international conference on computer vision*. pp. 1686–1695 (2023)
40. Paszke, A., Gross, S., Massa, F., Lerer, A., Bradbury, J., Chanan, G., Killeen, T., Lin, Z., Gimelshein, N., Antiga, L., et al.: Pytorch: An imperative style, high-performance deep learning library. *Advances in neural information processing systems* **32** (2019)
41. Radosavovic, I., Kosaraju, R.P., Girshick, R., He, K., Dollár, P.: Designing network design spaces. In: *Proceedings of the IEEE/CVF conference on computer vision and pattern recognition*. pp. 10428–10436 (2020)
42. Ren, J., Fort, S., Liu, J., Roy, A.G., Padhy, S., Lakshminarayanan, B.: A simple fix to mahalanobis distance for improving near-ood detection. arXiv preprint arXiv:2106.09022 (2021)
43. Shu, L., Xu, H., Liu, B.: Doc: Deep open classification of text documents. arXiv preprint arXiv:1709.08716 (2017)
44. Sun, Y., Guo, C., Li, Y.: React: Out-of-distribution detection with rectified activations. *Advances in neural information processing systems* **34**, 144–157 (2021)
45. Sun, Y., Ming, Y., Zhu, X., Li, Y.: Out-of-distribution detection with deep nearest neighbors. In: *International Conference on Machine Learning*. pp. 20827–20840. PMLR (2022)
46. Tukey, J.W., et al.: *Exploratory data analysis*, vol. 2. Springer (1977)
47. Van Horn, G., Mac Aodha, O., Song, Y., Cui, Y., Sun, C., Shepard, A., Adam, H., Perona, P., Belongie, S.: The inaturalist species classification and detection dataset. In: *Proceedings of the IEEE conference on computer vision and pattern recognition*. pp. 8769–8778 (2018)
48. Vaswani, A., Shazeer, N., Parmar, N., Uszkoreit, J., Jones, L., Gomez, A.N., Kaiser, Ł., Polosukhin, I.: Attention is all you need. *Advances in neural information processing systems* **30** (2017)
49. Wang, D., Shelhamer, E., Liu, S., Olshausen, B., Darrell, T.: Tent: Fully test-time adaptation by entropy minimization. arXiv preprint arXiv:2006.10726 (2020)

50. Wang, H., Li, Z., Feng, L., Zhang, W.: Vim: Out-of-distribution with virtual-logit matching. In: Proceedings of the IEEE/CVF conference on computer vision and pattern recognition. pp. 4921–4930 (2022)
51. Winkawaks: vit-tiny-patch16-224. <https://huggingface.co/WinKawaks/vit-tiny-patch16-224> (2023)
52. Xiao, J., Hays, J., Ehinger, K.A., Oliva, A., Torralba, A.: Sun database: Large-scale scene recognition from abbey to zoo. In: 2010 IEEE computer society conference on computer vision and pattern recognition. pp. 3485–3492. IEEE (2010)
53. Xu, K., Chen, R., Franchi, G., Yao, A.: Scaling for training time and post-hoc out-of-distribution detection enhancement. arXiv preprint arXiv:2310.00227 (2023)
54. Xu, P., Ehinger, K.A., Zhang, Y., Finkelstein, A., Kulkarni, S.R., Xiao, J.: Turkergaze: Crowdsourcing saliency with webcam based eye tracking. arXiv preprint arXiv:1504.06755 (2015)
55. Yang, J., Wang, H., Feng, L., Yan, X., Zheng, H., Zhang, W., Liu, Z.: Semantically coherent out-of-distribution detection. In: Proceedings of the IEEE/CVF International Conference on Computer Vision. pp. 8301–8309 (2021)
56. Yang, J., Wang, P., Zou, D., Zhou, Z., Ding, K., Peng, W., Wang, H., Chen, G., Li, B., Sun, Y., et al.: Openood: Benchmarking generalized out-of-distribution detection. *Advances in Neural Information Processing Systems* **35**, 32598–32611 (2022)
57. Yang, J., Zhou, K., Li, Y., Liu, Z.: Generalized out-of-distribution detection: A survey. *International Journal of Computer Vision* **132**(12), 5635–5662 (2024)
58. Yang, J., Zhou, K., Liu, Z.: Full-spectrum out-of-distribution detection. *International Journal of Computer Vision* **131**(10), 2607–2622 (2023)
59. Yang, P., Liang, J., Cao, J., He, R.: Auto: Adaptive outlier optimization for online test-time ood detection. arXiv preprint arXiv:2303.12267 (2023)
60. Yang, Y., Zhu, L., Sun, Z., Liu, H., Gu, Q., Ye, N.: Oodd: Test-time out-of-distribution detection with dynamic dictionary. In: Proceedings of the Computer Vision and Pattern Recognition Conference. pp. 30630–30639 (2025)
61. Yin, D., Gontijo Lopes, R., Shlens, J., Cubuk, E.D., Gilmer, J.: A fourier perspective on model robustness in computer vision. *Advances in Neural Information Processing Systems* **32** (2019)
62. Yu, F., Seff, A., Zhang, Y., Song, S., Funkhouser, T., Xiao, J.: Lsun: Construction of a large-scale image dataset using deep learning with humans in the loop. arXiv preprint arXiv:1506.03365 (2015)
63. Zagoruyko, S., Komodakis, N.: Wide residual networks. arXiv preprint arXiv:1605.07146 (2016)
64. Zhang, J., Inkawhich, N., Linderman, R., Chen, Y., Li, H.: Mixture outlier exposure: Towards out-of-distribution detection in fine-grained environments. In: Proceedings of the IEEE/CVF Winter Conference on Applications of Computer Vision. pp. 5531–5540 (2023)
65. Zhang, J., Yang, J., Wang, P., Wang, H., Lin, Y., Zhang, H., Sun, Y., Du, X., Li, Y., Liu, Z., et al.: Openood v1. 5: Enhanced benchmark for out-of-distribution detection. arXiv preprint arXiv:2306.09301 (2023)
66. Zhang, J., Fu, Q., Chen, X., Du, L., Li, Z., Wang, G., Han, S., Zhang, D., et al.: Out-of-distribution detection based on in-distribution data patterns memorization with modern hopfield energy. In: The Eleventh International Conference on Learning Representations (2022)
67. Zhou, B., Lapedriza, A., Khosla, A., Oliva, A., Torralba, A.: Places: A 10 million image database for scene recognition. *IEEE transactions on pattern analysis and machine intelligence* **40**(6), 1452–1464 (2017)

68. Zhu, J., Geng, Y., Yao, J., Liu, T., Niu, G., Sugiyama, M., Han, B.: Diversified outlier exposure for out-of-distribution detection via informative extrapolation. *Advances in Neural Information Processing Systems* **36**, 22702–22734 (2023)

# Appendix

## A Experimental details

### A.1 Datasets details

**CIFAR-100** CIFAR-100 [27] consists of 60,000 color images of size  $32 \times 32$  across 100 object classes, with 600 images per class. The dataset is divided into 50,000 training and 10,000 test samples. It includes diverse categories such as animals, vehicles, and everyday objects, and is commonly used for evaluating fine-grained image classification and representation learning. In our experiments, we use CIFAR-100 as the in-distribution dataset.

**SVHN** The Street View House Numbers (SVHN) dataset [36] contains real-world digit images collected from Google Street View. It consists of over 600,000 images, each containing a single digit cropped from house number signs, with a resolution of  $32 \times 32$ . The dataset includes 10 classes (digits 0–9) and is known for its relatively low intra-class variability and high image quality. We use SVHN as an out-of-distribution dataset in our evaluation.

**LSUN** The Large-scale Scene UNDERstanding (LSUN) dataset [62] contains millions of high-resolution images across various indoor and outdoor scene categories such as classroom, church, and bridge. In OOD detection benchmarks, a subset of LSUN is often used by resizing images to  $32 \times 32$  resolution to match CIFAR-style inputs. In our experiments, we use the resized LSUN images as out-of-distribution samples.

**iSUN** The iSUN dataset [54] consists of natural scene images collected for saliency prediction, containing various indoor and outdoor environments. It includes around 6,000 images, which are typically resized to  $32 \times 32$  for compatibility with CIFAR-based architectures. Due to its scene-centric content, iSUN is commonly used as an out-of-distribution dataset in image classification tasks. We follow prior works and use the resized version of iSUN for OOD evaluation.

**Textures** The Textures dataset [8], also known as the Describable Textures Dataset (DTD), contains 5,640 texture images spanning 47 categories such as striped, dotted, and cracked. The images are collected "in the wild" and exhibit a wide range of fine-grained, low-level patterns. Its low semantic content and high texture diversity make it a challenging out-of-distribution benchmark.

**ImageNet** ImageNet-1K dataset [10] contains 1.28M training images and 50K validation images across 1,000 object categories.

**ImageNet-O** ImageNet-O [23] is a curated out-of-distribution dataset containing 2,000 natural images that are semantically distinct from the 1,000 classes in ImageNet-1k. The images were collected to naturally lie outside the ImageNet taxonomy while maintaining comparable visual complexity. This dataset serves as a challenging benchmark for evaluating semantic OOD detection.

**SUN** The SUN dataset [52] is a large-scale scene understanding benchmark containing over 130,000 images across a wide variety of indoor and outdoor environments. It covers hundreds of semantic scene categories such as kitchen, mountain, and library. The diversity and scene-centric nature of SUN make it a strong candidate for out-of-distribution evaluation.

**iNaturalist** The iNaturalist dataset [47] contains high-resolution images of fine-grained natural categories such as plants, insects, birds, and mammals, collected from citizen science platforms. Due to its distinct domain and taxonomic diversity, iNaturalist is widely used as an out-of-distribution benchmark in vision tasks. Its semantic gap from object-centric datasets makes it a challenging OOD evaluation setting.

**Common corruptions** To evaluate robustness under covariate shift, we use a set of common image corruptions introduced by Hendrycks and Dietterich [19]. This benchmark includes 15 corruption types, grouped into noise (e.g., Gaussian noise, shot noise), blur (e.g., defocus, motion blur), weather (e.g., snow, fog), and digital distortions (e.g., JPEG compression, pixelation). We apply these corruptions to both in-distribution and out-of-distribution test samples to simulate realistic distribution shifts. Each corruption is applied at severity level 5, following the standard protocol used in prior robustness benchmarks.

## A.2 Baselines details

We introduce the baselines compared with *DART* and specify the hyperparameter used for implementation. The hyperparameter settings mainly follow the settings from the original paper.

**MSP** Maximum Softmax Probability [20] uses the highest softmax output value as the confidence score, assuming in-distribution samples yield higher confidence. We extract this directly from the classifier’s final layer.

**Energy** Energy-based detection [32] computes  $E(x) = -\log \sum_i \exp(f_i(x))$  from network logits, with lower values indicating in-distribution samples.  $T = 1.0$  is used for temperature scaling.

**Max logit** This method [18] uses the maximum pre-softmax logit value as the score, avoiding the normalization effect of softmax that may mask useful signals in relative logit magnitudes.

**GradNorm** GradNorm [24] measures the gradient magnitude of the loss with respect to the penultimate layer features. OOD samples tend to produce larger gradient norms. We use a temperature of 1.0 for all experiments.

**ViM** Virtual logit Matching [50] projects features into a null space and creates a virtual logit to enhance separation between ID and OOD samples. We set the dimension of the null space to 1000 for feature dimensions  $\geq 1500$ , to 512 for feature dimensions  $\geq 768$ , and to half the size of the feature dimensions otherwise.

**KNN** K-nearest neighbors [45] measures the distance to k-nearest neighbors in feature space, with OOD samples typically farther from ID samples. We use L2 normalization for features and set  $k=50$  for CIFAR-based experiments and  $k=200$  for ImageNet-based experiments.

**Mahalanobis distance** We implement both single-layer and ensemble versions of this method [29]. The single-layer version models class-conditional feature distributions using Gaussian distributions and measures the distance to the nearest class distribution, using the penultimate layer features. The ensemble version combines layer-wise scores from multiple network layers using pre-computed weights. These weights are learned by utilizing FGSM-perturbed inputs (magnitude 0.001) as synthetic OOD data and applying logistic regression (regularization strength  $C=1.0$ , max iterations=1000) to determine the contribution of each layer’s feature. We extract features for each layer or block depending on the model architecture.

**ODIN** ODIN [30] enhances OOD detection by applying input perturbations with temperature scaling to create a larger gap between ID and OOD confidence scores. FGSM epsilon values are set as 0.002 for both CIFAR-100 and ImageNet.

**ReAct** ReAct [44] truncates abnormally high hidden activations at test time, reducing model overconfidence on OOD data while preserving ID performance, thereby improving the separability between ID and OOD sample.

**SCALE** SCALE [53] is a post-hoc OOD detection method that applies activation scaling to penultimate features, thereby enlarging the separation between ID and OOD energy scores.

**ASH** ASH [11] prunes a large portion of late-layer activations (e.g., by top-K percentile) and either leaves the remaining values(ASH-P), binarizes them(ASH-B), or rescales them(ASH-S), then propagates the simplified representation through the network for scoring. We use ASH-P for performance comparison.

**RTL** RTL [14] fits a linear regression between OOD scores and network features at test time, calibrating base detector outputs to improve detection performance through test-time adaptation.

**NNGuide** NNGuide [39] leverages k-nearest neighbor distances in the feature space, scaled by the model’s confidence scores, to guide OOD detection by measuring how similar a test sample is to training samples while accounting for prediction confidence.

**CoRP** CoRP [15] applies cosine normalization followed by Random Fourier Features approximation of a Gaussian kernel, then computes PCA reconstruction errors for OOD detection.

**MDS++** MDS++ [35] enhances the standard Mahalanobis Distance Score by applying L2 normalization to feature representations before computing class-conditional statistics, thereby improving the geometric separation between ID and OOD samples in the normalized feature space.

**RMDS** RMDS (Relative Mahalanobis Distance Score) [42] computes relative Mahalanobis distances by comparing class-conditional scores against global background scores, effectively measuring how much a sample deviates from both class-specific and overall data distributions.

**RMDS++** RMDS++ [35] extends RMDS by incorporating L2 feature normalization before computing relative Mahalanobis distances, combining the benefits of normalized feature spaces with relative distance measurements to achieve more robust OOD detection.

### A.3 Evaluation model details

For CIFAR-100-based benchmark, we use the pre-trained WideResNet [63] with 40 layers and widen factor of 2 pretrained with AugMix [22] on clean CIFAR-100. The pretrained weights for this model is available from RobustBench [9].

For ImageNet-based benchmark, we use the pre-trained RegNetY-16GF [17] with the PyTorch checkpoint [40], which is trained on ImageNet and widely used for OOD detection task.

For evaluation on transformer-based architectures, we train two models: ViT-Tiny and Swin-Tiny. Both models are initialized with ImageNet-pretrained weights provided by HuggingFace model hub. We then fine-tune the model weights and classifier on the CIFAR-100 dataset. Training continues until each model reaches its target accuracy threshold (80% for ViT-Tiny and 85% for Swin-Tiny), after which early stopping is applied.

#### A.4 Evaluation details

For evaluation, we construct each test-time batch to contain 100 in-distribution (ID) samples and 100 out-of-distribution (OOD) samples, resulting in a fixed batch size of 200. We sample a total of 100 such test batches for each experimental setting. For each batch, we compute the AUROC and FPR@95TPR metrics, and report the final performance by averaging the values across all batches.

#### A.5 Compute resources

All experiments were conducted using NVIDIA RTX 3090 and RTX 4090 GPUs.

## B Method details

### B.1 Otsu algorithm

To automatically determine a threshold that separates two distributions (e.g., ID and OOD) based on their scalar scores, we adopt Otsu algorithm [38]. Originally proposed for image binarization, Otsu algorithm selects the threshold that minimizes the intra-class variance (or equivalently maximizes the inter-class variance) when partitioning a set of scalar values into two groups.

Given a histogram of score values, the algorithm exhaustively searches for the threshold  $\tau$  that minimizes the weighted sum of within-class variances:

$$\sigma_{\text{within}}^2(\tau) = \omega_0(\tau)\sigma_0^2(\tau) + \omega_1(\tau)\sigma_1^2(\tau), \quad (5)$$

where  $\omega_0(\tau)$  and  $\omega_1(\tau)$  are the probabilities of the two classes separated by threshold  $\tau$ , and  $\sigma_0^2(\tau)$ ,  $\sigma_1^2(\tau)$  are the corresponding class variances. This approach allows for an adaptive and data-driven determination of the decision threshold, without requiring access to ground-truth labels or distributional assumptions.

In our method, Otsu algorithm is applied to the distribution of OOD scores computed over each test-time batch. This enables unsupervised, on-the-fly threshold selection for distinguishing ID and OOD samples, and plays a critical role in decision-making process during inference.

### B.2 Tukey’s method

To ensure robust prototype estimation, we apply outlier filtering prior to aggregating the feature representations of test samples. Specifically, we adopt Tukey’s method, a non-parametric technique for identifying outliers based on the interquartile range (IQR) [46].

Given a set of distance values (e.g., Euclidean distances between features and their assigned prototype), we first compute the lower quartile ( $Q_1$ ) and upper quartile ( $Q_3$ ). The interquartile range is then defined as:

$$\text{IQR} = Q_3 - Q_1. \quad (6)$$

A sample is identified as a potential outlier if its score  $x$  satisfies:

$$x > Q_3 + 1.5 \cdot \text{IQR}. \quad (7)$$

We use Tukey’s method with an IQR factor of 1.5 throughout our experiments.

This filtering step is applied independently to the distance scores within each test-time batch, effectively removing extreme values that may otherwise distort the prototype update.

### B.3 Layer selection for *DART*

While it is possible to utilize the output of all intermediate layers for multi-layer aggregation, doing so incurs additional computational overhead. To reduce this overhead while still capturing hierarchical representations, we select a subset of representative layers at coarse block granularity, as specified in Table 6.

**Table 6:** Included layers list for *DART*

Model architecture	Included layers list
WideResNet-40-2	block1, block2, block3, fc
RegNetY-16GF	stem, trunk output {block1.block1-0, block1.block1-1, block2.block2-0 - block2.block2-3, block3.block3-0 - block3.block3-10, block4.block4-0}, fc
ViT-Tiny	vit.encoder.layer{0 - 11}, classifier
Swin-T	swin.encoder.layers{0.blocks.0, 0.blocks.1, 1.blocks.0, 1.blocks.1, 2.blocks.0 - 2.blocks.5, 3.blocks.0, 3.blocks.1}, classifier
ResNet-50	layer1, layer2, layer3, layer4, fc

## B.4 Algorithm of *DART*

---

### Algorithm 1 *DART*

---

**Require:** Pre-trained model  $f$ , layers  $L = \{1, \dots, L\}$ , EMA coefficient  $\alpha$

- 1: **Initialization using the first batch  $\mathcal{B}_1$ :**
  - 2: Let  $o = (o_1, \dots, o_C)$  be the logit vector
  - 3: Compute MSP:  $\text{MSP}_{1,i} = \max_c \frac{\exp(o_c)}{\sum_{j=1}^C \exp(o_j)}$
  - 4: Apply Otsu threshold  $\tau_1$  on MSP scores for pseudo-labeling:
 
$$\hat{y}_i = \begin{cases} \text{ID} & \text{if } \text{MSP}_{1,i} \geq \tau_1 \\ \text{OOD} & \text{otherwise} \end{cases}$$
  - 5: Partition features into  $\mathcal{B}_1^{ID}$  and  $\mathcal{B}_1^{OOD}$  based on  $\hat{y}_i$
  - 6: **for** each layer  $l \in L$  **do**
  - 7:   Initialize prototypes:
 
$$\bar{\mathbf{p}}_1^{(l),ID} = \frac{1}{|\mathcal{B}_1^{ID}|} \sum_{\mathbf{x}_{1,i} \in \mathcal{B}_1^{ID}} f_l(\mathbf{x}_{1,i}), \quad \bar{\mathbf{p}}_1^{(l),OOD} = \frac{1}{|\mathcal{B}_1^{OOD}|} \sum_{\mathbf{x}_{1,i} \in \mathcal{B}_1^{OOD}} f_l(\mathbf{x}_{1,i})$$
  - 8: **end for**
  - 9: **for** each batch  $\mathcal{B}_t$  **do**
  - 10:   **for** each layer  $l \in L$  **do**
  - 11:     **if**  $t \bmod n = 0$  **then**
  - 12:       Apply flip correction if prototypes are misaligned. Refer to Section 3.3 in main paper for details.
  - 13:     **end if**
  - 14:     Extract features:  $\mathbf{z}_{t,i}^{(l)} = f_l(\mathbf{x}_{t,i})$ ,  $\mathbf{x}_{t,i} \in \mathcal{B}_t$
  - 15:     Compute RDS:
 
$$\text{RDS}_i^{(l)} = 1 - \frac{\|\mathbf{z}_i^{(l)} - \bar{\mathbf{p}}_{t-1}^{ID,(l)}\|}{\|\mathbf{z}_i^{(l)} - \bar{\mathbf{p}}_{t-1}^{ID,(l)}\| + \|\mathbf{z}_i^{(l)} - \bar{\mathbf{p}}_{t-1}^{OOD,(l)}\|}$$
  - 16:     Apply Otsu threshold  $\tau_t$  on RDS scores for pseudo-labeling:
 
$$\hat{y}_i = \begin{cases} \text{ID} & \text{if } \text{RDS}_i^{(l)} \geq \tau_t \\ \text{OOD} & \text{otherwise} \end{cases}$$
  - 17:     Partition features into  $\mathcal{B}_t^{ID}$  and  $\mathcal{B}_t^{OOD}$  based on  $\hat{y}_i$
  - 18:     Apply Tukey’s method for outlier filtering:
 

Let  $s_i = \|\mathbf{z}_{t,i}^{(l)} - p^{\text{proto}}\|_2$ , where  $p^{\text{proto}}$  is the corresponding prototype

Filter out  $\mathbf{z}_{t,i}^{(l)}$  if  $s_i > Q_3 + k \cdot \text{IQR}$
  - 19:     Compute new centers:
 
$$\hat{\mathbf{p}}_t^{(l),ID} = \frac{1}{|\mathcal{B}_t^{ID}|} \sum_{\mathbf{x}_{t,i} \in \mathcal{B}_t^{ID}} f_l(\mathbf{x}_{t,i}), \quad \hat{\mathbf{p}}_t^{(l),OOD} = \frac{1}{|\mathcal{B}_t^{OOD}|} \sum_{\mathbf{x}_{t,i} \in \mathcal{B}_t^{OOD}} f_l(\mathbf{x}_{t,i})$$
  - 20:     Update prototypes with EMA:
 
$$\bar{\mathbf{p}}_t^{ID,(l)} = \alpha \cdot \hat{\mathbf{p}}_t^{ID,(l)} + (1-\alpha) \cdot \bar{\mathbf{p}}_{t-1}^{ID,(l)}, \quad \bar{\mathbf{p}}_t^{OOD,(l)} = \alpha \cdot \hat{\mathbf{p}}_t^{OOD,(l)} + (1-\alpha) \cdot \bar{\mathbf{p}}_{t-1}^{OOD,(l)}$$
  - 21:     **end for**
  - 22:    $\text{RDS}_{\text{multi}}(x_i) = \frac{1}{L} \sum_{l=1}^L \text{RDS}_i^{(l)}$
  - 23: **end for**
- 

## C Full Results

Here we show the full results for all OOD datasets which was abbreviated as average in the main manuscript due to space limits.

## C.1 Full CIFAR-100 Results with WideResNet on Clean Dataset

**Table 7:** OOD detection performance comparison with CIFAR-100 ID and the corresponding OODs. FPR@95TPR (%) is lower the better and AUROC (%) is higher the better. (Best: **bolded**, Second-best: underlined)

Clean													
Method	[Training dist.] informed	SVHN		Places365		LSUN		iSUN		Textures		Average	
		FPR95 ↓ AUROC ↑											
MSP	NO	79.32	77.27	80.37	74.99	78.39	76.91	81.23	74.56	82.55	72.70	80.37	75.29
Energy	NO	80.32	78.74	78.47	75.69	78.39	78.68	83.42	74.53	79.17	76.31	79.95	76.79
Max logit	NO	79.85	79.11	78.63	76.01	77.87	78.92	82.49	75.00	79.69	76.25	79.71	77.06
GradNorm	NO	96.80	44.47	94.81	51.36	98.22	32.12	98.48	30.97	86.31	59.18	94.92	43.62
ViM	YES	54.18	85.44	86.74	64.33	66.48	81.52	66.82	80.95	85.47	65.83	71.94	75.61
KNN	YES	63.34	86.06	80.09	73.38	66.57	84.85	72.86	80.60	74.54	80.89	71.48	81.16
Mahalanobis <sub>single</sub>	YES	77.75	75.58	90.94	59.26	69.56	80.02	70.64	78.54	91.15	56.50	80.01	69.98
Mahalanobis <sub>ensemble</sub>	YES	62.92	88.78	93.41	61.12	<b>13.12</b>	<b>97.34</b>	<u>16.44</u>	<u>96.55</u>	43.79	87.99	<u>45.94</u>	<u>86.36</u>
ODIN	NO	64.15	80.96	84.30	69.48	90.32	63.24	91.03	61.21	75.75	72.60	81.11	69.50
ReAct	YES	87.25	70.36	79.97	75.71	73.91	80.58	75.75	78.48	80.39	75.32	79.45	76.09
SCALE	NO	74.38	81.36	78.47	75.55	80.91	75.14	83.88	72.60	65.34	82.98	76.60	77.53
ASH	NO	79.20	79.65	79.96	75.11	81.64	77.12	85.45	73.20	75.96	78.72	80.44	76.76
RTL	NO	50.15	87.42	<u>73.23</u>	75.59	58.46	85.01	68.38	80.67	70.33	75.12	64.11	80.76
NNGuide	YES	86.85	71.34	87.71	67.73	94.66	59.74	95.50	57.33	73.01	75.32	87.55	66.29
CoRP	YES	<u>43.43</u>	<u>91.59</u>	86.30	68.31	82.53	77.18	80.56	77.13	<b>34.89</b>	<b>91.04</b>	65.54	81.16
MDS <sub>++</sub>	YES	83.59	81.25	85.42	70.98	84.16	77.33	86.64	73.88	90.00	74.15	85.96	75.52
RMDS	YES	68.73	85.23	77.53	<u>77.11</u>	53.64	88.28	57.46	85.64	83.13	76.29	67.90	82.51
RMDS <sub>++</sub>	YES	74.20	84.57	76.79	<b>77.67</b>	65.24	85.70	71.02	82.49	82.29	77.44	73.91	82.51
<b>DART</b>	NO	<b>9.64</b>	<b>97.67</b>	<b>70.00</b>	75.12	<u>30.24</u>	<u>91.49</u>	<b>14.79</b>	<b>96.62</b>	<u>40.91</u>	<u>88.02</u>	<b>33.12</b>	<b>89.78</b>

## C.2 Full ImageNet Results with RegNet on Clean Dataset

**Table 8:** OOD detection performance comparison with ImageNet ID and the corresponding OODs. FPR@95TPR (%) is lower the better and AUROC (%) is higher the better. (Best: **bolded**, Second-best: underlined)

Clean													
Method	[Training dist.] informed	IN-O		Places		SUN		iNaturalist		Textures		Average	
		FPR95 ↓ AUROC ↑											
MSP	NO	52.87	83.02	54.76	84.30	52.16	84.92	20.33	95.25	43.08	87.23	44.64	86.94
Energy	NO	57.59	76.17	48.11	81.05	41.17	85.04	<b>8.68</b>	97.49	35.69	87.87	38.25	85.52
Max logit	NO	52.30	78.42	47.22	82.29	41.65	85.60	9.50	97.43	34.57	88.39	37.05	86.43
GradNorm	NO	93.95	34.15	87.71	52.32	79.27	62.51	74.90	63.44	66.67	73.87	80.50	57.26
ViM	YES	30.21	93.82	71.37	82.93	72.21	83.42	50.70	90.12	58.42	87.70	56.58	87.60
KNN	YES	69.58	85.71	97.60	69.55	96.05	71.65	99.40	66.69	61.32	85.77	84.79	75.87
Mahalanobis <sub>single</sub>	YES	48.14	90.43	87.04	76.70	90.16	76.11	88.65	78.79	81.98	80.81	79.19	80.57
Mahalanobis <sub>ensemble</sub>	YES	<u>8.69</u>	<u>97.82</u>	78.62	81.37	77.80	82.59	88.75	77.80	<u>22.62</u>	<u>94.71</u>	55.30	86.86
ODIN	NO	60.40	82.05	71.28	76.69	68.97	77.47	47.64	88.78	55.90	84.33	60.84	81.86
ReAct	YES	97.32	53.19	90.93	65.47	85.13	72.83	74.11	85.74	84.53	76.10	86.40	70.67
SCALE	NO	52.97	77.70	<u>45.51</u>	82.83	<u>37.89</u>	86.79	8.72	97.46	29.96	90.30	<u>35.01</u>	87.02
ASH	NO	57.04	76.29	47.82	81.17	40.78	85.21	<b>8.43</b>	98.01	34.80	88.15	37.77	85.67
RTL	NO	52.60	79.13	49.71	83.58	48.01	82.53	21.53	90.75	39.67	85.22	42.30	84.24
NNGuide	YES	87.68	49.90	85.03	61.03	76.69	68.44	49.44	87.67	54.18	83.23	70.60	70.05
CoRP	YES	42.37	93.23	68.17	83.92	62.14	86.35	33.19	94.68	39.27	92.67	49.03	90.17
MDS <sub>++</sub>	YES	34.49	94.26	73.19	81.07	65.30	84.69	9.86	<b>98.01</b>	26.49	94.37	41.87	90.48
RMDS	YES	41.02	92.19	63.46	87.29	61.54	88.84	9.41	<u>97.54</u>	55.96	89.27	46.28	91.03
RMDS <sub>++</sub>	YES	57.33	90.42	73.07	85.76	70.16	87.53	17.70	96.44	61.79	88.50	56.01	89.73
<b>DART</b>	NO	<b>0.59</b>	<b>99.82</b>	<b>14.41</b>	<b>96.31</b>	<b>36.14</b>	<b>90.86</b>	20.71	95.28	<b>7.90</b>	<b>98.36</b>	<b>15.95</b>	<b>96.13</b>

### C.3 Full CIFAR-100 Results with ViT-Tiny

**Table 9:** OOD detection performance comparison with ViT-Tiny. We evaluate with CIFAR-100 ID, CIFAR-100-C csID and the corresponding OODs. (Best: **bolded**, Second-best: underlined)

Covariate Shifted													
Method	Training dist. informed	SVHN-C		Places365-C		LSUN-C		iSUN-C		Textures-C		Average	
		FPR95 ↓ AUROC ↑											
MSP	NO	88.32	54.65	89.98	57.41	89.13	60.20	90.96	57.75	89.39	55.15	89.56	57.03
Energy	NO	83.57	60.42	88.13	60.19	87.47	63.71	89.33	60.96	86.57	60.73	87.01	61.20
Max logit	NO	84.66	59.74	88.59	59.76	87.74	63.31	89.76	60.53	87.17	59.93	87.58	60.65
GradNorm	NO	89.95	62.39	89.89	56.74	92.07	54.39	92.37	53.47	83.40	65.13	89.54	58.42
ViM	YES	86.98	58.01	91.24	57.30	88.56	62.26	90.90	58.85	89.78	57.33	89.49	58.75
KNN	YES	90.16	56.65	90.34	54.45	90.01	60.53	92.23	55.79	87.99	56.64	90.15	56.81
Mahalanobis <sub>single</sub>	YES	97.65	32.82	96.87	34.13	96.77	33.42	97.27	31.31	97.54	30.30	97.22	32.40
Mahalanobis <sub>ensemble</sub>	YES	<u>37.91</u>	<b>90.30</b>	94.09	45.50	<u>61.56</u>	61.16	<u>61.78</u>	61.13	<b>53.29</b>	<b>71.68</b>	<u>61.73</u>	65.95
ODIN	NO	85.29	61.87	88.93	58.27	89.56	58.57	89.54	59.06	84.33	64.82	87.53	60.52
ReAct	YES	82.37	60.08	87.19	<u>61.31</u>	85.39	65.80	87.74	62.86	86.99	59.98	85.94	62.01
SCALE	NO	84.84	59.26	89.66	58.25	90.05	60.75	91.51	57.95	88.16	58.76	88.84	58.99
ASH	NO	92.41	58.90	91.56	55.26	93.51	52.40	93.88	51.33	88.62	62.12	92.00	56.00
RTL	NO	80.17	59.38	86.96	57.54	83.75	62.21	88.03	56.60	83.18	57.72	84.42	58.69
NNGuide	YES	86.45	59.03	87.05	59.69	86.04	64.58	88.36	61.35	84.53	61.21	86.49	61.17
CoRP	YES	88.45	59.62	89.92	56.64	87.28	63.92	89.22	59.97	86.69	59.10	88.31	59.85
MDS++	YES	77.22	67.31	<u>83.05</u>	<b>61.79</b>	78.16	<u>68.41</u>	80.03	<u>65.75</u>	72.31	<u>68.01</u>	78.15	<u>66.25</u>
RMDS	YES	76.29	65.91	87.26	60.66	84.90	65.54	87.27	61.98	77.44	63.73	82.63	63.56
RMDS++	YES	75.35	65.59	86.15	61.22	83.89	66.16	86.10	62.95	75.02	64.35	81.30	64.05
<i>DART</i>	NO	<b>36.44</b>	<u>71.92</u>	<b>67.29</b>	57.33	<b>25.08</b>	<b>80.93</b>	<b>31.67</b>	<b>75.50</b>	<u>60.90</u>	57.30	<b>44.28</b>	<b>68.60</b>
Clean													
Method	Training dist. informed	SVHN		Places365		LSUN		iSUN		Textures		Average	
		FPR95 ↓ AUROC ↑											
MSP	NO	62.06	82.50	78.47	74.69	70.48	81.33	74.85	78.79	65.92	81.63	70.36	79.79
Energy	NO	41.79	89.13	73.81	77.71	61.09	86.02	66.13	83.60	51.04	87.68	58.77	84.83
Max logit	NO	44.96	88.65	74.40	77.59	61.78	85.80	67.05	83.33	53.15	87.33	60.27	84.54
GradNorm	NO	70.09	81.30	83.25	69.27	85.99	72.71	87.16	70.48	65.14	82.44	78.33	75.24
ViM	YES	47.34	88.18	71.80	78.03	57.30	87.18	63.52	84.49	51.37	87.41	58.27	85.06
KNN	YES	60.23	83.70	79.73	69.78	65.70	83.28	72.82	77.93	58.29	83.19	67.35	79.58
Mahalanobis <sub>single</sub>	YES	97.62	31.26	94.24	47.56	96.96	31.19	97.67	27.57	95.40	40.26	96.38	35.57
Mahalanobis <sub>ensemble</sub>	YES	<u>13.93</u>	<u>97.14</u>	94.58	55.26	<u>3.03</u>	<u>99.06</u>	<u>3.93</u>	<u>98.93</u>	<b>30.44</b>	<b>91.63</b>	<u>29.18</u>	<u>88.40</u>
ODIN	NO	75.65	75.47	87.48	64.34	84.41	68.70	83.64	69.79	70.07	77.78	80.25	71.22
ReAct	YES	40.18	89.58	72.80	78.53	57.23	68.84	62.69	84.64	51.40	87.38	56.86	81.79
SCALE	NO	44.17	88.43	73.71	77.68	67.15	83.85	71.51	81.28	52.19	87.07	61.75	83.66
ASH	NO	77.25	79.20	83.45	69.11	86.72	71.52	88.41	69.02	70.01	81.14	81.17	74.00
RTL	NO	26.70	89.94	67.55	77.48	27.65	93.41	39.20	89.62	39.88	88.30	40.20	87.75
NNGuide	YES	47.09	87.22	76.40	74.95	60.59	85.51	66.31	82.58	51.10	86.91	60.30	83.43
CoRP	YES	61.85	85.00	80.76	73.19	64.51	85.81	68.88	82.48	60.42	85.68	67.28	82.43
MDS++	YES	39.14	88.84	66.54	78.57	42.39	90.18	48.78	87.41	36.66	90.59	46.70	87.12
RMDS	YES	36.21	89.32	<b>62.15</b>	<u>80.43</u>	47.61	88.92	55.13	85.97	38.81	90.00	47.98	86.93
RMDS++	YES	36.30	89.09	<u>62.64</u>	80.08	48.16	88.67	55.21	85.72	38.26	89.98	48.11	86.71
<i>DART</i>	NO	<b>3.24</b>	<b>99.23</b>	62.77	<b>81.73</b>	<b>0.85</b>	<b>99.80</b>	<b>1.04</b>	<b>99.74</b>	<u>35.00</u>	<u>91.04</u>	<b>20.58</b>	<b>94.31</b>

## C.4 Full CIFAR-100 Results with Swin-Tiny

**Table 10:** OOD detection performance comparison with Swin-Tiny. We evaluate with CIFAR-100 ID, CIFAR-100-C csID and the corresponding OODs. (Best: **bolded**, Second-best: underlined)

Covariate Shifted													
Method	Training dist. informed	SVHN-C		Places365-C		LSUN-C		iSUN-C		Textures-C		Average	
		FPR95 ↓ AUROC ↑											
MSP	NO	87.48	58.92	87.20	63.29	82.95	67.03	85.14	64.75	84.33	62.97	85.42	63.39
Energy	NO	81.88	67.29	86.20	64.20	78.30	71.63	81.65	68.08	73.47	70.53	80.30	68.35
Max logit	NO	83.72	66.10	86.30	64.38	79.40	71.16	82.44	67.79	77.63	69.22	81.90	67.73
GradNorm	NO	82.38	68.38	89.90	62.00	80.76	72.92	79.68	<u>73.52</u>	<u>61.12</u>	<b>80.40</b>	78.77	71.44
ViM	YES	95.84	51.26	94.98	50.17	97.60	46.77	98.04	43.00	98.22	37.61	96.94	45.76
KNN	YES	82.69	68.02	87.62	60.94	82.50	67.52	85.40	62.77	83.06	65.31	84.25	64.91
Mahalanobis <sub>single</sub>	YES	98.23	38.79	97.74	41.80	99.32	32.79	99.36	30.22	99.13	21.86	98.76	33.09
Mahalanobis <sub>ensemble</sub>	YES	97.17	44.72	97.94	39.09	99.35	31.32	99.38	29.27	99.14	24.34	98.60	33.75
ODIN	NO	80.78	66.20	89.74	59.86	91.86	58.65	91.08	59.38	70.96	74.06	84.88	63.63
ReAct	YES	78.42	69.44	85.84	65.20	76.79	73.35	78.67	71.44	64.09	76.25	76.76	71.14
SCALE	NO	79.13	69.57	86.21	65.09	76.71	73.93	78.22	72.28	63.15	<u>76.96</u>	76.68	71.57
ASH	NO	78.65	70.33	87.57	63.95	77.48	73.87	78.64	72.06	62.42	76.76	76.95	71.39
RTL	NO	86.72	57.38	86.72	62.68	79.41	69.61	83.11	65.84	82.61	62.58	83.71	63.62
NNGuide	YES	78.56	<u>72.74</u>	<u>84.64</u>	<u>67.62</u>	<u>73.65</u>	<u>76.11</u>	<u>76.30</u>	73.44	69.52	76.99	76.53	<u>73.38</u>
CoRP	YES	84.83	67.05	89.32	59.20	85.16	65.79	86.98	61.99	84.56	64.22	86.17	63.65
MDS++	YES	<u>72.36</u>	<b>75.29</b>	88.15	60.55	78.41	69.66	79.70	66.70	61.44	76.79	<u>76.01</u>	69.80
RMDS	YES	91.82	59.47	91.80	56.76	89.66	61.30	91.74	57.40	91.61	55.75	91.33	58.14
RMDS++	YES	89.90	63.59	90.80	58.82	85.84	64.50	88.39	60.72	85.74	61.41	88.13	61.81
<i>DART</i>	NO	<b>44.90</b>	70.99	<b>57.62</b>	<b>75.48</b>	<b>14.28</b>	<b>95.53</b>	<b>24.97</b>	<b>87.74</b>	<b>52.74</b>	76.66	<b>38.90</b>	<b>81.28</b>
Clean													
Method	Training dist. informed	SVHN		Places365		LSUN		iSUN		Textures		Average	
		FPR95 ↓ AUROC ↑											
MSP	NO	59.06	86.09	69.83	79.17	58.09	85.76	62.11	83.42	51.72	87.13	60.16	84.31
Energy	NO	35.88	91.83	58.64	83.16	38.61	91.40	44.35	88.95	27.80	93.67	41.06	89.80
Max logit	NO	37.54	91.54	58.73	83.04	39.41	91.10	45.02	88.66	29.86	93.28	42.11	89.52
GradNorm	NO	85.31	61.74	83.37	67.78	70.06	80.46	68.41	80.33	51.02	82.32	71.63	74.53
ViM	YES	83.71	80.08	93.84	62.22	96.72	63.50	97.19	59.52	93.54	65.96	93.00	66.26
KNN	YES	31.60	93.26	66.75	80.31	46.95	89.67	53.14	86.22	31.23	93.09	45.93	88.51
Mahalanobis <sub>single</sub>	YES	97.07	59.75	98.46	43.08	99.67	35.81	99.72	33.62	98.43	33.27	98.67	41.11
Mahalanobis <sub>ensemble</sub>	YES	96.51	64.83	98.40	43.33	99.57	38.31	99.65	36.58	97.99	44.61	98.42	45.53
ODIN	NO	89.89	67.25	95.52	59.39	97.62	57.25	97.04	57.87	75.93	76.50	91.20	63.65
ReAct	YES	42.84	90.56	58.78	82.17	38.80	91.42	42.60	89.57	25.89	93.83	41.78	89.51
SCALE	NO	49.51	87.94	62.13	81.02	40.86	91.00	44.03	89.32	27.67	93.21	44.84	88.50
ASH	NO	54.51	85.90	67.96	79.09	46.42	89.69	48.93	88.02	32.31	92.14	50.03	86.97
RTL	NO	43.25	87.35	70.99	74.76	44.41	87.35	51.83	84.40	44.03	87.30	50.90	84.23
NNGuide	YES	37.51	91.82	<b>56.58</b>	<b>84.28</b>	33.61	<u>93.04</u>	<u>38.34</u>	<u>91.40</u>	<u>24.15</u>	<u>94.75</u>	38.04	<u>91.06</u>
CoRP	YES	41.14	92.32	68.66	80.55	50.94	89.81	55.48	87.22	35.63	92.77	50.37	88.53
MDS++	YES	<u>30.97</u>	<u>93.67</u>	<u>56.68</u>	<u>83.95</u>	<u>33.31</u>	92.98	39.00	90.82	<b>16.43</b>	<b>96.28</b>	<u>35.28</u>	<b>91.54</b>
RMDS	YES	52.84	89.57	64.26	82.37	52.70	88.97	59.42	86.09	40.78	91.23	54.00	87.65
RMDS++	YES	47.14	90.76	58.64	83.56	44.55	90.16	50.92	87.55	33.78	92.48	47.01	88.90
<i>DART</i>	NO	<b>7.27</b>	<b>97.88</b>	77.97	64.13	<b>6.31</b>	<b>98.52</b>	<b>6.68</b>	<b>98.49</b>	<u>61.06</u>	81.14	<b>31.86</b>	88.03

## C.5 Full ImageNet Results with ResNet-50

**Table 11:** OOD detection performance comparison with ResNet-50 on ImageNet-based benchmark. Results on covariated shifted dataset are the average of all 15 corruptions with severity level 5. (Best: **bolded**, Second-best: underlined)

Covariate Shifted													
Method	Training dist. informed	ImageNet-O-C		Places-C		SUN-C		iNaturalist-C		Textures-C		Average	
		FPR95 ↓ AUROC ↑											
MSP	NO	86.14	55.60	86.79	63.17	84.84	65.27	77.89	69.62	88.52	54.85	84.84	61.70
Energy	NO	82.16	58.92	89.03	61.29	87.91	63.58	86.44	64.52	88.05	55.85	86.72	60.83
Max logit	NO	83.88	57.81	87.57	63.00	85.79	65.42	81.49	68.07	88.02	55.87	85.35	62.03
GradNorm	NO	76.86	64.58	70.84	77.06	65.23	80.51	51.36	85.62	67.11	74.14	66.28	76.38
ViM	YES	95.64	38.92	99.50	17.64	99.65	14.90	99.94	8.60	96.94	25.14	98.33	21.04
KNN	YES	83.81	63.63	90.93	55.23	91.12	56.45	95.20	45.36	61.31	73.33	84.47	58.80
MDS <sub>single</sub>	YES	95.14	38.80	99.52	18.75	99.67	15.95	99.93	9.60	96.20	27.69	98.09	22.16
MDS <sub>ensemble</sub>	YES	79.71	62.76	92.44	42.67	92.17	41.57	94.26	33.49	64.44	62.83	84.60	48.66
ODIN	NO	76.69	68.04	<u>25.14</u>	<u>92.96</u>	<u>22.70</u>	<u>93.69</u>	<u>27.84</u>	<u>92.22</u>	38.11	85.81	<u>38.10</u>	<u>86.54</u>
ReAct	YES	82.24	59.09	84.47	67.56	82.92	69.76	80.76	70.72	84.85	59.33	83.05	65.29
SCALE	NO	79.10	63.07	79.87	70.76	76.10	74.05	63.83	79.72	75.88	68.39	74.96	71.20
ASH	NO	80.51	61.30	87.83	63.20	86.48	65.88	82.64	68.22	84.77	60.05	84.45	63.73
RTL	NO	82.27	57.85	76.94	71.71	73.29	74.47	64.06	78.47	81.14	59.14	75.54	68.33
NNGuide	YES	73.91	67.80	68.11	77.74	62.29	81.42	50.54	85.43	57.13	78.16	62.40	78.11
CoRP	YES	75.89	<u>73.38</u>	75.07	73.16	71.42	76.37	67.32	78.15	44.54	<u>86.27</u>	66.85	77.47
MDS++	YES	<b>63.76</b>	<b>77.47</b>	81.50	66.32	79.47	69.03	66.54	77.67	<u>36.03</u>	<b>88.92</b>	65.46	75.88
RMDS	YES	90.38	50.24	95.39	44.28	95.88	42.31	96.52	45.83	85.80	50.46	92.79	46.62
RMDS++	YES	77.40	64.63	86.31	58.47	85.77	58.86	78.16	68.26	61.45	73.34	77.82	64.71
<b>DART</b>	NO	<u>73.52</u>	58.78	<b>2.46</b>	<b>99.34</b>	<b>1.06</b>	<b>99.59</b>	<b>1.18</b>	<b>99.61</b>	<b>23.75</b>	79.75	<b>20.39</b>	<b>87.41</b>
Clean													
Method	Training dist. informed	ImageNet-O		Places		SUN		iNaturalist		Textures		Average	
		FPR95 ↓ AUROC ↑											
MSP	NO	64.81	75.42	56.33	85.09	53.18	85.97	36.95	91.68	53.73	83.95	53.00	84.42
Energy	NO	55.18	82.01	42.09	89.64	34.38	91.54	25.30	94.38	33.96	90.49	38.18	89.61
Max logit	NO	55.09	81.85	42.79	78.62	35.50	91.39	23.88	95.05	35.07	90.28	38.47	87.44
GradNorm	NO	55.97	78.38	47.85	87.45	42.19	88.60	24.01	94.34	42.17	86.85	42.44	87.12
ViM	YES	56.20	77.62	42.62	86.49	31.60	90.55	21.81	94.30	33.31	89.08	37.11	87.61
KNN	YES	<u>11.09</u>	97.01	72.62	83.16	72.49	84.40	82.54	79.21	<u>16.31</u>	<u>96.53</u>	51.01	88.06
MDS <sub>single</sub>	YES	11.10	95.67	54.71	87.07	45.46	90.53	78.67	76.90	19.89	94.97	41.97	89.03
MDS <sub>ensemble</sub>	YES	30.76	88.27	95.87	62.81	95.47	62.19	97.37	50.94	49.44	86.03	73.78	70.05
ODIN	NO	18.70	94.49	94.09	64.38	93.09	64.67	96.72	51.10	29.60	91.41	66.44	73.21
ReAct	YES	16.84	95.44	36.62	89.54	34.89	89.80	38.99	88.92	35.50	88.30	32.57	90.40
SCALE	NO	50.55	84.83	37.29	91.44	30.29	93.06	17.02	96.40	31.67	92.22	33.36	91.59
ASH	NO	42.77	87.82	<u>32.37</u>	<u>92.47</u>	24.55	94.22	<b>10.87</b>	<b>97.60</b>	19.80	94.77	26.07	93.38
RTL	NO	56.98	75.34	42.41	86.56	36.48	87.81	23.85	91.29	38.71	85.14	39.69	85.23
NNGuide	YES	38.59	88.32	<b>28.59</b>	<b>93.10</b>	<u>20.02</u>	<u>95.18</u>	17.82	96.20	21.11	94.17	<u>25.23</u>	<u>93.39</u>
CoRP	YES	30.01	89.25	64.00	84.28	55.98	87.82	83.16	73.97	23.66	94.53	51.36	85.97
MDS++	YES	14.92	<u>97.16</u>	61.42	84.92	49.94	88.97	33.84	93.72	<b>1.69</b>	<b>99.49</b>	32.36	92.85
RMDS	YES	61.88	88.56	87.73	79.15	88.16	80.24	65.98	90.30	51.95	88.58	71.14	84.97
RMDS++	YES	56.42	86.76	75.65	82.07	73.61	83.96	36.83	93.50	29.65	91.97	54.43	87.65
<b>DART</b>	NO	<b>0.60</b>	<b>99.83</b>	33.90	89.31	<b>15.90</b>	<b>95.77</b>	<u>14.29</u>	<u>96.46</u>	23.68	94.78	<b>17.67</b>	<b>95.23</b>

## D Theoretical Analysis

We analyze why the discriminative axis  $\mathbf{d} = \boldsymbol{\mu}_{\text{ID}} - \boldsymbol{\mu}_{\text{OOD}}$  is an effective OOD detector and why its norm is large. Throughout,  $\hat{\mathbf{z}}(x) \in \mathbb{R}^K$  denotes the post-BN feature vector with  $K$  channels, and BN normalizes each channel  $k$  by frozen ID statistics:  $\hat{Z}_k(x) = \gamma_k \frac{(Z_k(x) - \mu_{\text{ID},k})}{\sqrt{\sigma_{\text{ID},k}^2 + \epsilon}} + \beta_k$ . Since  $\epsilon \approx 10^{-5}$ , the post-BN ID variance satisfies  $v_{\text{ID},k}^2 \triangleq \text{Var}_{x \sim P_{\text{ID}}}[\hat{Z}_k(x)] = \gamma_k^2 \frac{\sigma_{\text{ID},k}^2}{\sigma_{\text{ID},k}^2 + \epsilon} \approx \gamma_k^2$ .

### D.1 Separation Bound for the Discriminative Axis

Consider the centered projection score  $\tilde{s}(x) = \mathbf{d}^\top (\hat{\mathbf{z}}(x) - \boldsymbol{\mu}_{\text{OOD}})$ . The projected class means are

$$\mathbb{E}[\tilde{s} \mid \text{ID}] = \|\mathbf{d}\|^2, \quad \mathbb{E}[\tilde{s} \mid \text{OOD}] = 0, \quad (8)$$

giving an exact mean gap of  $\|\mathbf{d}\|^2$ . The projected variance is  $\text{Var}[\tilde{s} \mid C] = \mathbf{d}^\top \boldsymbol{\Sigma}_C \mathbf{d}$ . We assume that the within-class variance remains controlled along the discriminative direction:

*Assumption A1 (bounded directional variance).* There exists a constant  $\kappa > 0$  such that

$$\mathbf{d}^\top \boldsymbol{\Sigma}_C \mathbf{d} \leq \kappa \|\mathbf{d}\|^2, \quad C \in \{\text{ID}, \text{OOD}\}. \quad (9)$$

This condition constrains only the variance along the single direction  $\mathbf{d}$ , without imposing structure on the full covariance matrix. A sufficient condition is bounded operator norm:  $\|\boldsymbol{\Sigma}_C\|_{\text{op}} \leq \kappa$  implies A1 immediately.

Using the midpoint threshold  $\tau = \|\mathbf{d}\|^2/2$ , Chebyshev’s inequality yields

$$P(\tilde{s} < \tau \mid \text{ID}) \leq \frac{4\kappa}{\|\mathbf{d}\|^2}, \quad (10)$$

because the ID mean is  $\|\mathbf{d}\|^2$ , and similarly

$$P(\tilde{s} \geq \tau \mid \text{OOD}) \leq \frac{4\kappa}{\|\mathbf{d}\|^2}, \quad (11)$$

because the OOD mean is 0. Therefore, the overlap decreases as  $\mathcal{O}(1/\|\mathbf{d}\|^2)$ : larger norm of the discriminative axis directly improves separation between ID and OOD along the projected score.

*Fisher optimality of the discriminative axis.* Let  $\mathbf{S}_W = \boldsymbol{\Sigma}_{\text{ID}} + \boldsymbol{\Sigma}_{\text{OOD}}$  be the within-class scatter matrix. The SNR of the projection along  $\mathbf{d}$  equals the Fisher criterion:  $\text{SNR} = \|\mathbf{d}\|^4 / (\mathbf{d}^\top \mathbf{S}_W \mathbf{d}) = J(\mathbf{d})$ . In general, the Fisher-optimal direction is  $\mathbf{w}^* \propto \mathbf{S}_W^{-1} \mathbf{d}$ , which need not align with  $\mathbf{d}$ . However, when the within-class scatter is approximately diagonal with comparable entries — i.e.  $\mathbf{S}_W \approx 2\gamma^2 \mathbf{I}$  — the inverse acts as a uniform rescaling and  $\mathbf{S}_W^{-1} \mathbf{d} \propto \mathbf{d}$ , so the discriminative axis coincides with the Fisher-optimal direction.

## D.2 Why the Discriminative Axis Norm Is Large

The  $k$ -th component of  $\mathbf{d}$  in post-BN space decomposes as

$$d_k = \frac{\gamma_k}{\sqrt{\sigma_{\text{ID},k}^2 + \epsilon}} \underbrace{(\mathbb{E}[Z_k | \text{ID}] - \mathbb{E}[Z_k | \text{OOD}])}_{\Delta_k} = \lambda_k \Delta_k, \quad (12)$$

where  $\lambda_k = \gamma_k / \sqrt{\sigma_{\text{ID},k}^2 + \epsilon}$  is the BN scaling factor and  $\Delta_k$  is the pre-BN mean shift. The axis norm is  $\|\mathbf{d}\|^2 = \sum_{k=1}^K \lambda_k^2 \Delta_k^2$ .

Any  $\lambda_k > 1$  means BN amplifies the pre-BN mean shift in channel  $k$ , and the key observation is that this amplification *compounds across  $K$  channels*: even  $\bar{\lambda}$  modestly above 1 can yield  $\|\mathbf{d}\|^2 \gg 4\kappa$  when  $K$  is large.

In the final BN layer of a pretrained ResNet-50 ( $K=2048$ ), the measured scaling factors have mean  $\bar{\lambda} \approx 23.3$  with a coefficient of variation of 5.7%, placing the bound deep in the non-trivial regime: moderate per-channel shifts accumulate across 2048 channels into a large  $\|\mathbf{d}\|^2$ , directly tightening the bound in Eq. (10).

## E Effect of EMA $\alpha$

We employ an exponential moving average (EMA) to update the prototype, where the smoothing coefficient  $\alpha$  is treated as an only hyperparameter of *DART*. To examine the sensitivity of our method to this hyperparameter, we conduct an ablation study on the CIFAR-100-C vs. SVHN-C and ImageNet-C vs. iNaturalist-C benchmark, and report the results as AUROC(%) in Table 12. Results in Table 12 demonstrates that our method is robust to the choice of the EMA coefficient  $\alpha$ .

**Table 12:** The effect of EMA  $\alpha$  on the performance of *DART*

$\alpha$	0.5	0.6	0.7	0.8	0.9	std.
CIFAR-100-C vs. SVHN-C	78.79	78.68	78.84	78.58	78.11	$\pm 0.29$
ImageNet-C vs. iNaturalist-C	93.18	93.18	93.18	93.18	93.19	$\pm 0.00$

## F Impact of Flip Correction

To quantitatively assess the impact of flip correction, we compare with a variant that does not perform flip correction, *DART-NoFlip*, using CIFAR-100-C as the csID dataset. As shown in Table 13, flip correction improves the performance of our method.



*DART* with multi-layer fusion, using CIFAR-100-C as csID and Textures-C as csOOD. See Figure 11 for all results.

This extended analysis reveals that the best-performing layer is highly shift-dependent: under noise-type corruptions such as Gaussian or impulse noise, deeper layers suffer larger degradation, whereas under corruptions such as motion blur and brightness, earlier layers are more severely affected and later layers remain relatively more informative. As a result, relying on any single fixed layer for OOD detection is brittle when the covariate shift type is unknown a priori. In contrast, the fused *DART* score achieves both the highest mean performance and the most stable behavior: averaged over all corruption types, *DART* not only outperforms every single-layer variant, but also exhibits substantially smaller variation than the strongest single-layer baseline (Block3), with standard deviation 0.1661 versus 0.2582 for Block3. These results quantitatively support our claim that multi-layer fusion is crucial for robust OOD detection under unpredictable covariate shift.

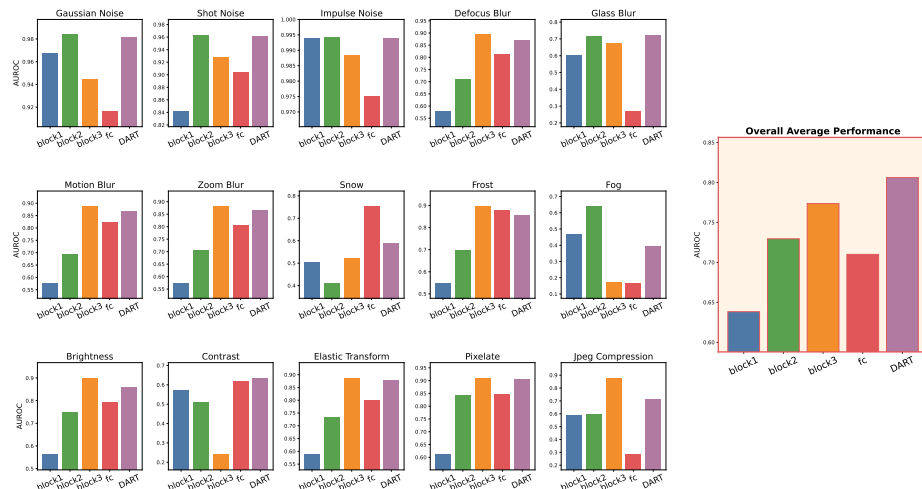


Fig. 11: Impact of Multi-layer Fusion (CIFAR-100-C vs. Textures-C)

## H Sensitivity to the ID/OOD Ratio

Table 14 shows that *DART* remains robust across a broad range of batch compositions, achieving consistently strong performance when the ID proportion is between 0.2 and 0.8. We use ResNet-50 with ImageNet as ID and iNaturalist as OOD. This highlights an important strength of our method: it does not rely on a narrowly tuned ID/OOD mixture and generalizes well under moderate batch imbalance. Nevertheless, we observe a performance drop in more extreme cases, such as when the ID proportion reaches 0.9. Because *DART* leverages the internal

geometry of each batch, a sufficient number of both ID and OOD samples is generally needed to stably initialize and preserve the discriminative axis. When OOD samples become overly scarce, the estimated axis can become less reliable and more sensitive.

**Table 14:** The sensitivity to the ID proportion

$\ \mathcal{B}_t^I\ /\ \mathcal{B}_t\ $	0.1	0.2	0.3	0.4	0.5	0.6	0.7	0.8	0.9
FPR95	32.31	20.15	16.12	15.50	14.29	12.14	12.45	23.02	68.57
AUROC	84.67	94.81	96.33	96.05	96.46	97.04	96.80	93.88	70.31

Importantly, this issue can be mitigated through axis stabilization strategy which combines balanced initialization with adaptive and conservative axis updates. To verify this, we conduct an additional experiment in Tab. 15, where the discriminative axis is initialized using five balanced batches and then updated with a large EMA coefficient  $\alpha = 0.95$ . Under this setting, the performance degradation is substantially reduced even in highly imbalanced regimes that can occur in practice when OOD samples are particularly scarce, including ID proportions of 0.9, 0.95, and 0.99. These results suggest that the performance drop of *DART* under extreme imbalance is largely associated with instability in axis estimation, which can be effectively controlled with proper initialization and conservative updates. A promising direction for future work is to adapt the EMA coefficient to the batch composition, rather than using a fixed value, in order to further improve axis stability under severe imbalance.

**Table 15:** The sensitivity to the ID proportion with axis stabilization strategy

$\ \mathcal{B}_t^I\ /\ \mathcal{B}_t\ $	0.9	0.95	0.99
FPR95	14.00	16.96	30.18
AUROC	96.21	95.34	89.20

## I System overhead

We measure wall-clock inference time for all methods on the same device, after the backbone forward pass, and only for the OOD-score computation (Figure 12). Concretely, we report the total time required to process 100 mini-batches of size 200 (20k test samples in total), using RegNetY-16GF. Under this protocol, *DART* falls into the group of fast methods: it is markedly faster than recent baselines

such as RTL, NNGuide, and MDS-based variants, which require regression fitting, KNN-style searches, or repeated Mahalanobis evaluations.

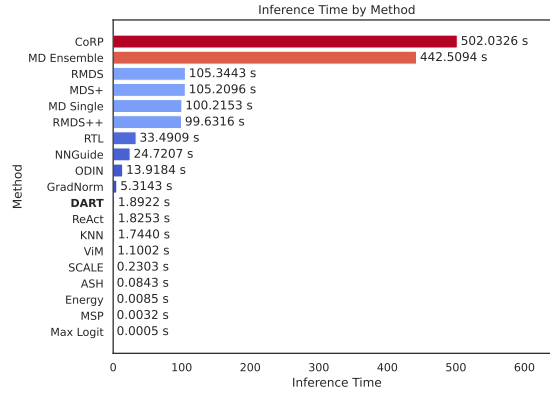


Fig. 12: Inference time

## J Visualization of ROC curves

We visualize the ROC curves of our method and the baselines across several evaluation settings. As shown in Figure 13, *DART* achieves lower FPR in this high-TPR region even when overall AUROC is comparable to baselines. Since real-world deployment requires maintaining high ID acceptance while minimizing false alarms, FPR@95TPR better captures the performance that matters in practice.

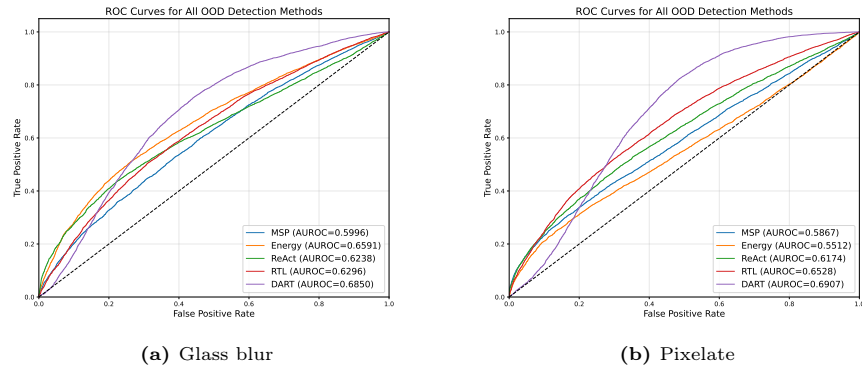
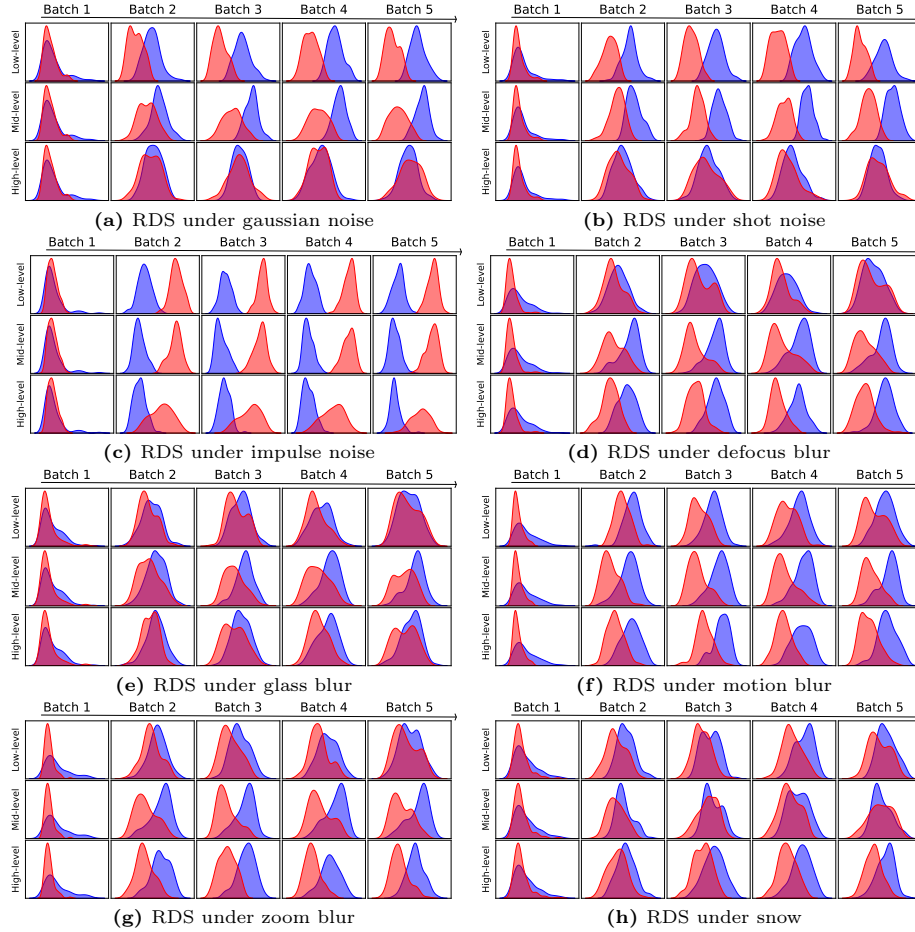


Fig. 13: ROC curves for CIFAR-100 vs. LSUN under different corruptions

## K Extended RDS distribution visualizations

In the main paper, we present representative visualizations of RDS distributions for a subset of corruption types, to illustrate how ID and OOD samples are separated across different feature levels. These visualizations support our observation that the most discriminative layer can vary depending on the type of corruption. For completeness, we provide the full set of visualizations covering all 15 corruption types in this appendix.

### K.1 RDS distribution visualizations



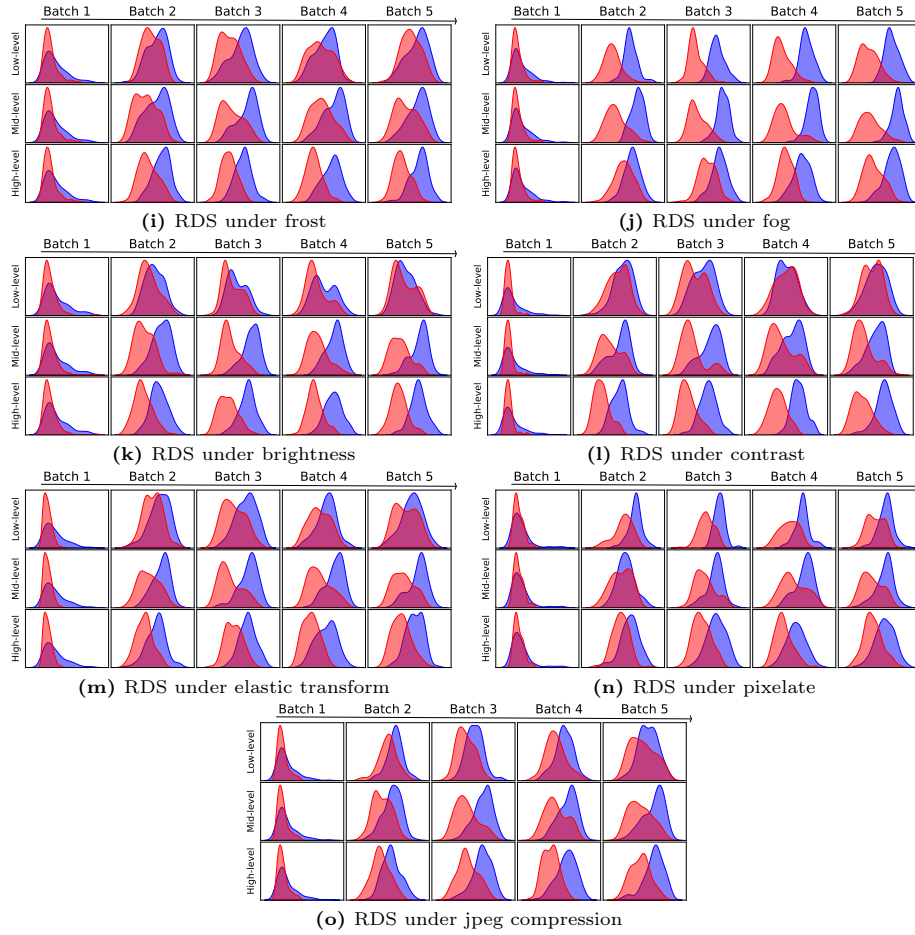


**Fig. 14:** Full corruptions visualizations for RDS distributions. Each plot shows at different network depths (low, mid, high-level) through five sequential batches. The visualizations reveal how different corruption types affect RDS separability at specific network layers.